

Contents lists available at [ScienceDirect](https://www.sciencedirect.com)

## Comput. Methods Appl. Mech. Engrg.

journal homepage: [www.elsevier.com/locate/cma](http://www.elsevier.com/locate/cma)

# Output probability distribution estimation of stochastic static and dynamic systems using Laplace transform and maximum entropy

Yang Zhang <sup>a</sup>, Chao Dang <sup>b</sup>\*, Jun Xu <sup>a,c</sup>\*\*, Michael Beer <sup>d,e,f</sup>

<sup>a</sup> College of Civil Engineering, Hunan University, Changsha 410082, China

<sup>b</sup> Chair for Reliability Engineering, TU Dortmund University, Leonhard-Euler-Str. 5, Dortmund 44227, Germany

<sup>c</sup> State Key Laboratory of Bridge Engineering Safety and Resilience, Hunan University, Changsha 410082, China

<sup>d</sup> Institute for Risk and Reliability, Leibniz University Hannover, Hannover 30167, Germany

<sup>e</sup> Department of Civil and Environmental Engineering, University of Liverpool, Liverpool L69 3GH, United Kingdom

<sup>f</sup> International Joint Research Center for Resilient Infrastructure & International Joint Research Center for Engineering Reliability and Stochastic Mechanics, Tongji University, Shanghai 200092, China

## ARTICLE INFO

### Keywords:

Stochastic system  
Probability distribution estimation  
Complex distribution  
Laplace transform  
Inverse Laplace transform  
Maximum entropy

## ABSTRACT

Effectively estimating output probability distributions in stochastic static and dynamic systems with a limited number of simulations is a significant challenge, especially for complex distributions with multi-modality and heavy tails. To address this challenge, this work explores the potential of the Laplace Transform (LT) and its inversion. First, the statistical information embedded in the derivatives of the LT is analysed, establishing the theoretical foundation for recovering output probability distributions. Subsequently, a novel analytical expression for the response probability density function (PDF) is derived by decomposing its inverse LT (ILT) using Euler's formula. Building on the numerically estimated LT, a non-parametric numerical solution, termed the Numerical Decomposed ILT (NDILT) algorithm, is developed to flexibly estimate the main body of complex PDFs with limited samples. Second, the Taylor expansion of the real component of LT (RCLT) reveals its rich statistical content. Exploiting this property, another parametric method, the LT-based Maximum Entropy Method (LT-MEM), is proposed, incorporating estimated RCLT as constraints of the maximum entropy principle. By solving an optimization problem, LT-MEM can effectively reconstruct complex PDFs across their entire distribution domain using a small sample size. The proposed methods rediscover and harness the power of the LT and ILT to reconstruct complex-shaped probability distributions, offering a valuable alternative. Parameter selection strategies for NDILT and LT-MEM are provided, and their robust accuracy is validated through analytical and numerical examples across various challenging distributions.

## 1. Introduction

The output probability distributions of stochastic static and dynamic systems fully characterize the probabilistic properties of the system's response, enabling the calculation of key statistical information, such as moments and tail probabilities. Accurate estimation of the output probability distributions, while accounting for input uncertainties in both system parameters and external excitations, is therefore essential for applications in uncertainty characterization, reliability analysis, engineering design optimization, etc.

\* Corresponding author.

\*\* Corresponding author at: College of Civil Engineering, Hunan University, Changsha 410082, China.

E-mail addresses: [chao.dang@tu-dortmund.de](mailto:chao.dang@tu-dortmund.de) (C. Dang), [xujun86@hnu.edu.cn](mailto:xujun86@hnu.edu.cn) (J. Xu).

<https://doi.org/10.1016/j.cma.2025.117887>

Received 11 December 2024; Received in revised form 9 February 2025; Accepted 24 February 2025

Available online 13 March 2025

0045-7825/© 2025 The Authors. Published by Elsevier B.V. This is an open access article under the CC BY license (<http://creativecommons.org/licenses/by/4.0/>).

In practice, output probability distributions often exhibit complex features like non-Gaussian behaviour, heavy tails, and multi-modality, attributed to the complex probability distributions of input random variables and the highly nonlinear behaviour of systems. Additionally, the computational models for simulating real-world systems are often expensive to evaluate, which means a limited number of output samples are affordable for estimating the output probability distribution. These factors pose significant challenges for accurately and efficiently reconstructing the output distributions. Numerous methods for output probability distribution estimation of stochastic systems have been developed, which generally fall into two categories: non-parametric and parametric methods.

Non-parametric estimation avoids specifying a functional form for the response probability distribution of interest, providing flexibility by modelling data directly [1,2]. Common non-parametric methods include histogram-based approaches, Kernel Density Estimation (KDE) [3–5], B-spline-based techniques [1,6,7], and the Probability Density Evolution Method (PDEM) [8–12], etc. Histogram methods offer insights into the distributions of data derived from practical observations or sampling techniques, such as Monte Carlo Simulation (MCS) and its variants [13–15]. However, they lack an analytical Probability Density Function (PDF) representation and may lose details due to discretization, particularly when samples are limited. KDE [3–5] is a popular non-parametric approach, known for simplicity and effectiveness, though its performance hinges on selecting an optimal bandwidth, which can be challenging [4,7]. Additionally, although KDE handles complex distributions well, it requires large samples to achieve the desired level of accuracy, especially for the distribution tail [2,16,17]. B-spline-based estimators, due to their localized support, limit each data point's influence to adjacent basis elements, attracting recent attention [1,6,7]. However, some B-spline methods do not guarantee non-negativity or normalization of the PDF [7] and are challenging for problems with high-dimensional random inputs [1]. PDEM, originally introduced by Li and Chen [8], is effective in both static and dynamic applications [9–12,18]. Additionally, the direct probability integral method is developed to reconstruct PDFs using a weighted KDE, showing promising results [19–21], but shares KDE's limitations [16,22]. Recently developed excellent non-parametric methods, such as the characteristic function inversion method [16], harmonic transform-based techniques [22,23] and Bayesian active learning method [24], effectively recover complex distributions but may require further exploration for high-dimensional cases.

Parametric methods, particularly moment-based approaches, are widely used to estimate PDFs by leveraging the statistical moments of target random variables. Traditional methods, including the Pearson system [25], shifted generalized lognormal distribution [26], Hermite model [27], and saddlepoint approximation [28], etc., typically reconstruct PDFs using the first four moments. However, these methods are generally limited to uni-modal distributions with regular shapes [16]. The moment-based Maximum Entropy Method (MEM) [29–33] has emerged as a powerful alternative for reconstructing unknown distributions. Standard MEM, known as Integer Moment-based MEM (IM-MEM), uses integer moments for PDF estimation, but this can be insufficient for capturing tails accurately with low-order moments, while higher-order moments may induce numerical instability [30]. The Fractional Moment-based MEM (FM-MEM) [34] was introduced to address these limitations by using fractional moments as constraints, offering greater flexibility and enhanced accuracy. To ensure robustness, the Fractional Exponential Moment-based MEM (FEM-MEM), which combines MEM with the Laplace transform (LT), was developed and widely applied [35–38]. Additionally, MEM with integer or fractional moments has also been extended to estimate multi-modal distributions [39,40]. Despite MEM's success in response probability distribution estimation, reconstructing complex PDFs, especially those with multiple modes or heavy tails, remains challenging [22,41,42].

FEM-MEM has been extensively used for probability distribution reconstruction based on the LT along the real axis [37,38,43], but applications of the LT in the complex domain for this purpose remain largely unexplored. Given the widespread use of LT in various scientific disciplines [44], numerous numerical Inverse LT (ILT) methods have been developed, as detailed in Refs. [45,46], etc. However, these methods typically assume a known LT, which limits their practical application in reconstructing probability distributions. Efforts have been made to recover some specific PDFs with heavy tails via ILT [47]. Thus, the LT and its inversion hold significant potential for estimating complex-shaped probability distributions, meriting further exploration.

The main objective of this work is to develop LT-based methods for accurate and efficient estimation of output probability distributions in stochastic static and dynamic systems, especially for distributions with complex shapes. The contributions of this study are threefold:

- (1) This work explores the potential of the LT and ILT for estimating output probability distributions with complex shapes in stochastic systems, offering a powerful alternative to capture intricate probabilistic information of output driven by complex input uncertainties and highly nonlinear system behaviour;
- (2) A new analytic expression for the output PDF over the real domain is derived, named the Decomposed ILT (DILT) method, by decomposing its ILT in the complex domain. The DILT method is supported by its numerical algorithm, Numerical DILT (NDILT), which facilitates highly flexible and computationally efficient reconstruction of the main body of complex-shaped output probability distributions using a limited number of system simulations;
- (3) Additionally, this work reveals that the real part of the LT in the complex domain encapsulates substantial statistical information about the probability distribution. Building on this insight, a method termed LT-MEM is proposed, integrating the Real Component of LT (RCLT) with the MEM. This method enables accurate reconstruction of complex-shaped probability distributions across their entire distribution range, leveraging the superior characteristics of the RCLT.

This work proposes an effective framework for reconstructing output probability distributions in stochastic static and dynamic systems. It comprises a non-parametric method, NDILT, and a parametric approach, LT-MEM. These methods leverage powerful mathematical tools, i.e., the LT in the complex domain and its inversion, offering a novel and robust alternative for estimating probability distributions with complex shapes. The basic workflow of the proposed methods is illustrated in Fig. 1. The rest of

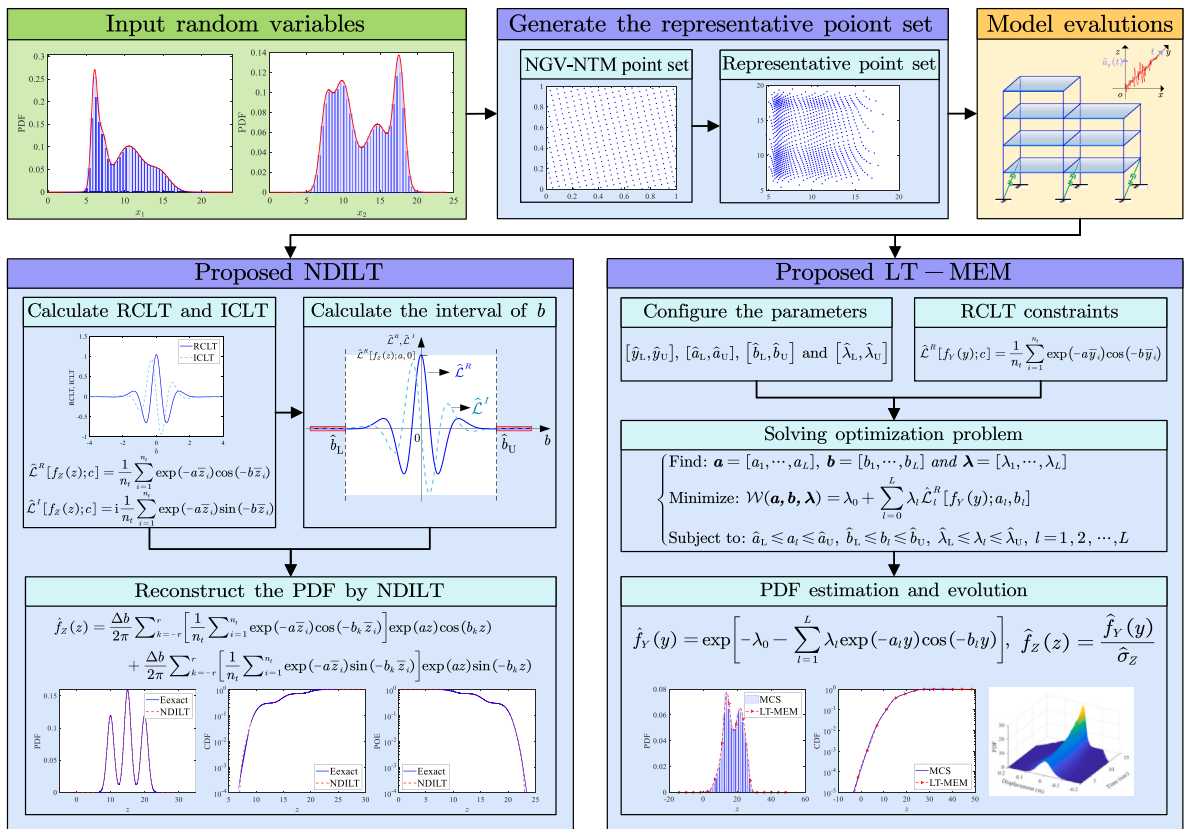


Fig. 1. Basic workflow of the proposed methods.

this paper is structured as follows. In Section 2, the problem to be addressed in this study is formulated. Section 3 and Section 4 present the proposed DILT and LT-MEM, respectively. Four test examples in Section 5 demonstrate the effectiveness of the proposed methods, and Section 6 provides some concluding remarks.

**2. Problem formulation**

Let  $\Theta = [\theta_1, \theta_2, \dots, \theta_d] \in \Omega_\Theta \subseteq \mathbb{R}^d$  represent a vector of  $d$  continuous random variables, defined over the probability space  $(\Omega_\Theta, \mathcal{F}, \mathbb{P})$ . Here,  $\Omega_\Theta$  is the sample space,  $\mathcal{F}$  is a  $\sigma$ -algebra on  $\Omega_\Theta$ , and  $\mathbb{P} : \Omega_\Theta \rightarrow [0, 1]$  is the probability measure on  $(\Omega_\Theta, \mathcal{F})$ . These input variables  $\Theta$  characterize the uncertainties associated with both system parameters and external excitations in the stochastic systems under consideration. For a static system, the output of interest, denoted as  $Z$ , can then be defined by a deterministic computational model, represented as:

$$Z = G(\Theta), \tag{1}$$

where  $G(\cdot) : \mathbb{R}^d \rightarrow \mathbb{R}$  is a deterministic mapping that represents a physical system. For a dynamic system, the response at a given time instant can also be expressed as in Eq. (1).

Since the input parameters of the concerned system are random variables, the output response  $Z$  is also a random variable. Its PDF, denoted as  $f_Z(z)$ , can be expressed as

$$f_Z(z) = \int_{\Omega_\Theta} \gamma(z - G(\theta)) f_\Theta(\theta) d\theta, \tag{2}$$

where  $\gamma(\cdot)$  is the Dirac delta function and  $f_\Theta(\theta)$  denotes the joint PDF of  $\Theta$ .

The output PDF  $f_Z(z)$  completely characterizes the probabilistic properties of the system’s response, serving as a crucial foundation for uncertainty characterization, reliability analysis, and related applications. However, in most real-world scenarios, the analytical solution of the output PDF  $f_Z(z)$  is not available, necessitating the development of numerical methods to estimate  $f_Z(z)$ . On the other hand, computational models for simulating real-world systems are often computationally expensive, limiting the number of output samples for estimating the output probability distributions. This constraint causes many state-of-the-art numerical methods to struggle with low flexibility and accuracy, particularly when dealing with complex-shaped distributions. To address the research gap, effective LT-based methods for PDF estimation are proposed in the following two sections.

### 3. NDILT for probability density estimation

The LT can capture complete statistical information about a random variable, making it an invaluable tool for reconstructing its PDF. Building on the LT, this section proposes a new method for estimating unknown PDFs. It begins with a concise overview of the foundational concepts and properties of the LT. Next, a new analytical expression for reconstructing PDF is derived by decomposing the ILT, forming the core of the proposed DILT method. Finally, the corresponding numerical algorithm, referred to as the NDILT, is presented to facilitate the practical implementation of the DILT method.

#### 3.1. Definition of the LT and its inversion

The bilateral LT of output PDF  $f_Z(z)$ , denoted as function  $\mathcal{L}[f_Z(z); c] : \mathbb{C} \mapsto \mathbb{C}$ , can be defined as

$$\mathcal{L}[f_Z(z); c] = \int_{-\infty}^{\infty} f_Z(z) \exp(-cz) dz, \tag{3}$$

where  $c$  is a complex number, i.e.,  $c = a + ib$  with real numbers  $a$  and  $b$ , and  $i = \sqrt{-1}$  is the imaginary unit. For clarity, all instances of LT in this paper refer exclusively to the bilateral LT.

In Eq. (3),  $f_Z(z)$  and its LT  $\mathcal{L}[f_Z(z); c]$  are interconnected, such that knowing one enables the recovery of the other [48]. The existence of LT is guaranteed if there exist constants  $h^-, h^+ \in \mathbb{R}$ , such that [48]

$$0 \leq \int_0^{\infty} f_Z(z) \exp(-h^+z) dz < \infty, 0 \leq \int_{-\infty}^0 f_Z(z) \exp(-h^-z) dz < \infty. \tag{4}$$

Then, the existence domain of the LT can be defined as  $\{c : a \in (-\infty, h_{\max}^-) \cap (h_{\min}^+, \infty)\}$ , where  $h_{\max}^-$  denotes the maximum value of  $h^-$  and  $h_{\min}^+$  represents the minimum value of  $h^+$ . In this paper, the concerned output PDFs are assumed to have a non-empty existence domain.

Accordingly, the ILT, denoted by  $\bar{\mathcal{L}}[f_Z(z); c]$ , is defined through the following complex integral:

$$f_Z(z) = \bar{\mathcal{L}}[f_Z(z); c] = \frac{1}{2\pi i} \int_{a-i\infty}^{a+i\infty} \exp(cz) \mathcal{L}[f_Z(z); c] dc. \tag{5}$$

It should be noted that the integration in Eq. (5) is performed along the imaginary axis, and the result is independent of the fixed real part  $a$  [16,22,49,50]. Then, Eq. (5) can be rewritten as

$$f_Z(z) = \bar{\mathcal{L}}[f_Z(z); c] = \frac{1}{2\pi} \int_{-\infty}^{+\infty} \exp(cz) \mathcal{L}[f_Z(z); c] db. \tag{6}$$

For the output  $Z$ , its raw moments are encoded within the derivatives of the  $\mathcal{L}[f_Z(z); c]$  at the origin, given by [51]

$$\mathbb{E}[Z^K] = (-1)^K \left. \frac{d^K \mathcal{L}[f_Z(z); c]}{dc^K} \right|_{c=0}, \tag{7}$$

where  $\mathbb{E}[\cdot]$  denotes the expectation operator,  $\mathbb{E}[Z^K]$  represents the  $K$ th raw moment of  $Z$ . Clearly, the LT retains complete statistical features of a probability distribution, which can subsequently be retrieved via the ILT.

#### 3.2. Proposed DILT method

Eq. (6) offers a conceptually straightforward way to reconstruct the PDF  $f_Z(z)$ . However, despite its theoretical clarity, solving Eq. (6) is challenging due to the integration involving a complex-valued integrand. To address this, this section re-derives the analytic expression for the interested PDF  $f_Z(z)$  by decomposing the ILT, termed the DILT method, and provides the corresponding numerical algorithm, called the NDILT algorithm, to facilitate practical implementation, as detailed below. In the DILT method,  $f_Z(z)$  is reformulated as an integral of a real-valued function over the real domain, providing an efficient alternative for computing output probability distributions.

##### 3.2.1. New analytic expression of PDF using DILT

First, according to the Euler's formula,  $\exp(-cz)$  can be expressed as follows

$$\exp(-cz) = \exp(-az) [\cos(-bz) + i \sin(-bz)]. \tag{8}$$

By substituting Eq. (8) into Eq. (3), the LT  $\mathcal{L}[f_Z(z); c]$  can be rewritten as

$$\begin{aligned} \mathcal{L}[f_Z(z); c] &= \int_{-\infty}^{\infty} f_Z(z) \exp(-az) [\cos(-bz) + i \sin(-bz)] dz \\ &= \mathcal{L}^R[f_Z(z); c] + \mathcal{L}^I[f_Z(z); c], \end{aligned} \tag{9}$$

where  $\mathcal{L}^R[f_Z(z); c]$  and  $\mathcal{L}^I[f_Z(z); c]$  represent the real and imaginary components of the LT, denoted as RCLT and ICLT, respectively, which are defined as follows

$$\mathcal{L}^R[f_Z(z); c] = \mathbb{E}[\exp(-aZ) \cos(-bZ)] = \int_{-\infty}^{\infty} f_Z(z) \exp(-az) \cos(-bz) dz, \tag{10}$$

$$\mathcal{L}^I [f_Z(z); c] = \mathbb{E} [\exp(-aZ)i \sin(-bZ)] = \int_{-\infty}^{\infty} f_Z(z) \exp(-az)i \sin(-bz) dz. \tag{11}$$

After that, substituting Eqs. (8), (10) and (11) into Eq. (6), the ILT (Eq. (6)) can be further decomposed as

$$\begin{aligned} f_Z(z) &= \tilde{\mathcal{L}} [f_Z(z); c] \\ &= \frac{1}{2\pi} \int_{-\infty}^{+\infty} \mathcal{L}^R [f_Z(z); c] \exp(az) \cos(bz) db \\ &\quad + \frac{1}{2\pi} \int_{-\infty}^{+\infty} \mathcal{L}^I [f_Z(z); c] \exp(az)i \sin(bz) db \\ &\quad + \frac{1}{2\pi} \int_{-\infty}^{+\infty} \mathcal{L}^R [f_Z(z); c] \exp(az)i \sin(bz) db \\ &\quad + \frac{1}{2\pi} \int_{-\infty}^{+\infty} \mathcal{L}^I [f_Z(z); c] \exp(az) \cos(bz) db, \end{aligned} \tag{12}$$

It can be observed that Eq. (12) effectively decomposes the integral in Eq. (6) into its real and imaginary components. Specifically, the first two terms on the right-hand side of Eq. (12) represent the real part of  $f_Z(z)$ , while the last two terms correspond to the imaginary part. Considering that  $f_Z(z)$  is a real-valued function, a new analytic expression for  $f_Z(z)$  is derived by omitting the imaginary part in Eq. (12), as follows

$$\begin{aligned} f_Z(z) &= \frac{1}{2\pi} \int_{-\infty}^{+\infty} \mathcal{L}^R [f_Z(z); c] \exp(az) \cos(bz) db \\ &\quad + \frac{1}{2\pi} \int_{-\infty}^{+\infty} \mathcal{L}^I [f_Z(z); c] \exp(az) i \sin(bz) db. \end{aligned} \tag{13}$$

Due to the complexity of Eq. (13), deriving an analytical solution remains challenging, even when  $\mathcal{L}^R [f_Z(z); c]$  and  $\mathcal{L}^I [f_Z(z); c]$  are known. Moreover, if the LT of  $f_Z(z)$  is unknown, Eq. (13) cannot be solved directly due to the presence of  $f_Z(z)$  in the integrand. Consequently, it is necessary to pursue a numerical solution, which is detailed below.

### 3.2.2. Numerical algorithm for DILT

The inner integrals of Eq. (13), namely RCLT  $\mathcal{L}^R [f_Z(z); c]$  and ICLT  $\mathcal{L}^I [f_Z(z); c]$ , are defined as expected values. Consequently, these integrals can be estimated numerically from samples of  $Z$ , denoted as  $\bar{z} = (\bar{z}_1, \bar{z}_2, \dots, \bar{z}_i, \dots, \bar{z}_{n_t})$ , where  $i = 1, 2, \dots, n_t$ . The numerical estimates, denoted as  $\hat{\mathcal{L}}^R [f_Z(z); c]$  and  $\hat{\mathcal{L}}^I [f_Z(z); c]$ , respectively, are given as follows

$$\hat{\mathcal{L}}^R [f_Z(z); c] = \frac{1}{n_t} \sum_{i=1}^{n_t} \exp(-a\bar{z}_i) \cos(-b\bar{z}_i), \tag{14}$$

$$\hat{\mathcal{L}}^I [f_Z(z); c] = i \frac{1}{n_t} \sum_{i=1}^{n_t} \exp(-a\bar{z}_i) \sin(-b\bar{z}_i). \tag{15}$$

The numerical evaluations of  $\mathcal{L}^R [f_Z(z); c]$  (Eq. (14)) and  $\mathcal{L}^I [f_Z(z); c]$  (Eq. (15)) are critical for recovering the unknown PDF  $f_Z(z)$ , as any induced errors may adversely propagate into the PDF calculation. Therefore, careful selection of the sampling methods for evaluating  $\hat{\mathcal{L}}^R [f_Z(z); c]$  (Eq. (14)) and  $\hat{\mathcal{L}}^I [f_Z(z); c]$  (Eq. (15)) is essential. To balance accuracy and efficiency, this paper employs a low-discrepancy point selection strategy, called the New Generating Vector-based Number-Theoretical Method (NGV-NTM) [52], with details provided in Appendix A. Once the representative point set of the input random variables  $\Theta$ , denoted as  $\mathcal{P}_\theta = \{\theta_i = (\theta_{i,1}, \theta_{i,2}, \dots, \theta_{i,d}), i = 1, 2, \dots, n_t\}$ , is obtained by NGV-NTM, repeatedly deterministic model evaluations, i.e.,  $Z = G(\Theta)$ , are conducted to generate the corresponding output samples of  $Z$ , i.e.,  $\bar{z}$ . These samples can then be substituted into Eqs. (14) and (15) to compute the numerical  $\hat{\mathcal{L}}^R [f_Z(z); c]$  and  $\hat{\mathcal{L}}^I [f_Z(z); c]$ .

By substituting Eqs. (14) and (15) into Eq. (13), the numerical estimation of the PDF  $f_Z(z)$ , referred to as the NDILT algorithm, is obtained as follows

$$\begin{aligned} f_Z(z) &\approx \hat{f}_Z(z) \\ &= \frac{\Delta b}{2\pi} \sum_{k=-r}^r \left[ \frac{1}{n_t} \sum_{i=1}^{n_t} \exp(-a\bar{z}_i) \cos(-b_k \bar{z}_i) \right] \exp(az) \cos(b_k z) \\ &\quad + \frac{\Delta b}{2\pi} \sum_{k=-r}^r \left[ \frac{1}{n_t} \sum_{i=1}^{n_t} \exp(-a\bar{z}_i) \sin(-b_k \bar{z}_i) \right] \exp(az) \sin(-b_k z), \end{aligned} \tag{16}$$

where  $\hat{f}_Z(z)$  represents the estimated PDF;  $\Delta b$  denotes the discretization step;  $b_k = k\Delta b$  and  $2r + 1$  denotes the total number of discretizations.

The numerical PDF  $\hat{f}_Z(z)$  is expressed in Eq. (16) as a summation of a finite number of terms. Therefore, the number of these terms must be determined carefully. Specifically, the RCLT  $\mathcal{L}^R [f_Z(z); c]$  and ICLT  $\mathcal{L}^I [f_Z(z); c]$ , for a fixed value of  $a$ , approach zero as  $|b|$  increases due to their decaying nature. Once the values of the RCLT and ICLT become sufficiently small, their contribution to the accuracy of the numerical PDF is minimal and can thus be neglected. Moreover, both RCLT and ICLT exhibit the same

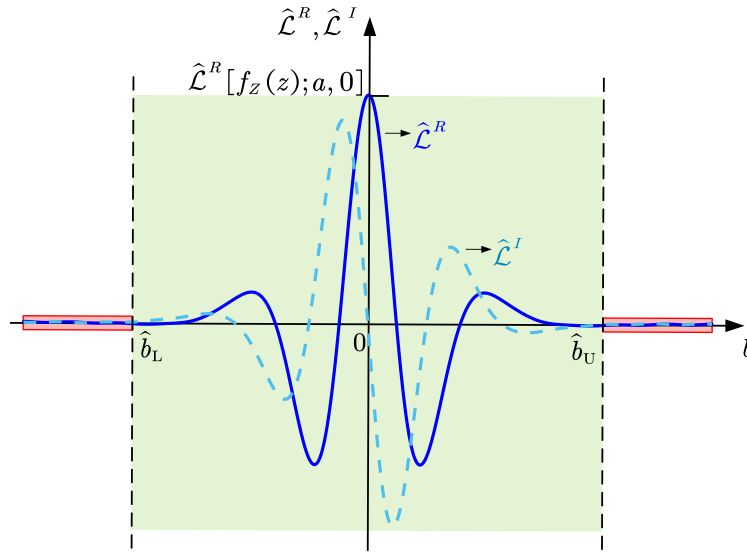


Fig. 2. Schematic diagram of the estimated interval  $[\hat{b}_L, \hat{b}_U]$ . (For interpretation of the references to colour in this figure legend, the reader is referred to the web version of this article.)

convergence behaviour. Therefore, to determine the number of cumulative terms and mitigate the effects of tail estimation errors in the numerical RCLT and ICLT, an estimated finite interval of  $b$ , denoted as  $[\hat{b}_L, \hat{b}_U] = [-\hat{b}_L, \hat{b}_U]$ , where  $\hat{b}_L$  and  $\hat{b}_U$  represent the estimated lower and upper bounds of  $b$ , should be specified in accordance with the following formula:

$$\underline{b_U} \leq \hat{b}_U \leq \overline{b_U}, \tag{17}$$

where

$$\begin{cases} \overline{b_U} = \min \left\{ \bar{b} \mid \forall b \in (\bar{b}, +\infty), \left| \hat{\mathcal{L}}^R [f_Z(z); a, b] \right| \leq \rho_1 \hat{\mathcal{L}}^R [f_Z(z); a, 0] \right\}, \bar{b} \in [0, +\infty) \\ \underline{b_U} = \min \left\{ \bar{b} \mid \forall b \in (\bar{b}, +\infty), \left| \hat{\mathcal{L}}^R [f_Z(z); a, b] \right| \leq \rho_2 \hat{\mathcal{L}}^R [f_Z(z); a, 0] \right\}, \bar{b} \in [0, +\infty) \end{cases}, \tag{18}$$

where  $\hat{\mathcal{L}}^R [f_Z(z); a, b] = \hat{\mathcal{L}}^R [f_Z(z); c]$ ,  $\hat{\mathcal{L}}^R [f_Z(z); a, 0]$  is the value of  $\hat{\mathcal{L}}^R [f_Z(z); a, b]$  with  $b = 0$ ;  $a$  is set to  $a = -0.01$ ;  $\rho_1$  and  $\rho_2$  are empirically set to  $\rho_1 = 0.001$  and  $\rho_2 = 0.05$ , respectively. The schematic diagram of calculating the interval  $[\hat{b}_L, \hat{b}_U]$  is shown in Fig. 2.

Utilizing the parameters  $\rho_1$  and  $\rho_2$  ( $\rho_1 > \rho_2 > 0$ ), the range of admissible values for  $\hat{b}_U$  is determined by Eq. (18). Subsequently, a specific value of  $\hat{b}_U$  is selected from the interval  $[b_U, \overline{b_U}]$  using Eq. (17), thereby ensuring both robustness and flexibility, while mitigating the propagation of tail errors of numerical LT. In this regard, Eq. (17) defines the abscissa intervals for the main body of the numerical RCLT  $\hat{\mathcal{L}}^R [f_Z(z); c]$  and ICLT  $\hat{\mathcal{L}}^I [f_Z(z); c]$ , see the green part in Fig. 2, for values that can be accurately computed, while discarding tail regions (see the red part in Fig. 2) that converge to zero but introduce estimation errors. The numerical RCLT and ICLT within the interval  $[\hat{b}_L, \hat{b}_U]$  can then be applied in Eq. (16) to estimate the PDF. In Eq. (16), a small value of  $a = -0.01$  is selected for the real part parameter  $a$  to prevent divergence in the numerical integration. The numerical integration step size,  $\Delta b$ , should be sufficiently small to ensure the accuracy of the estimated PDF, depending on the problem at hand, yet not so small as to incur unnecessary computational costs. In this work,  $\Delta b$  is set to 0.01 to strike a balance between accuracy and efficiency. Furthermore, the parameter  $r$  is defined as  $r = \hat{b}_U / \Delta b$ .

### 3.3. Step-by-step procedure of the proposed NDILT algorithm

The implementation procedure of the NDILT algorithm is illustrated in Fig. 3, with the detailed steps outlined as follows:

- Step 1:** Determine the number of input random variables  $d$  and number of samples  $n_i$ , and then generate the corresponding representative point set  $\mathcal{P}_\theta = \{\theta_i = (\theta_{i,1}, \theta_{i,2}, \dots, \theta_{i,d}), i = 1, 2, \dots, n_i\}$  using NGV-NTM, as described in Appendix A.
- Step 2:** Substitute each point from the representative point set  $\mathcal{P}_\theta$  into the response function  $Z = G(\Theta)$ , and perform repeatedly deterministic model evaluations to obtain the output samples  $\bar{z} = (\bar{z}_1, \bar{z}_2, \dots, \bar{z}_i, \dots, \bar{z}_{n_i}), i = 1, 2, \dots, n_i$ , of  $Z$ .
- Step 3:** Substitute samples  $\bar{z}$  of  $Z$  into Eqs. (14) and (15) to compute the numerical ICLT  $\hat{\mathcal{L}}^I [f_Z(z); c]$  and RCLT  $\hat{\mathcal{L}}^R [f_Z(z); c]$ .

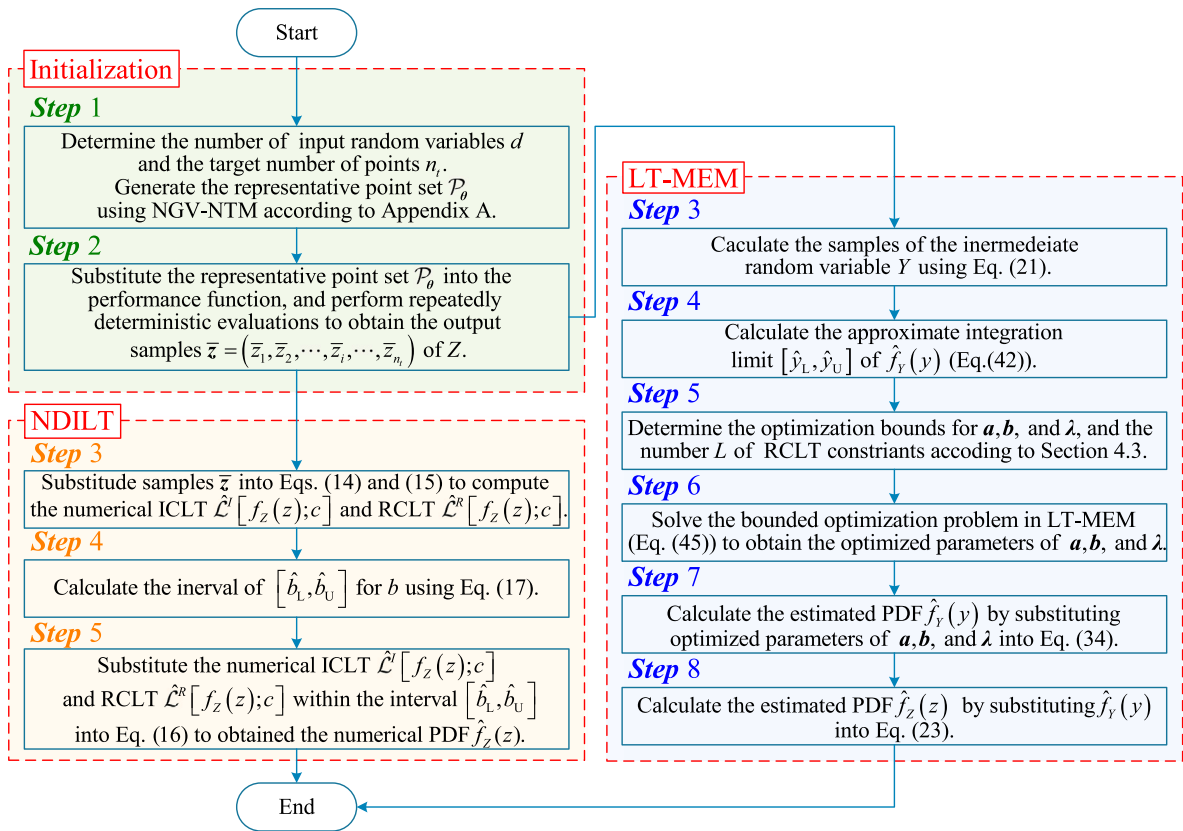


Fig. 3. Flowchart of the proposed NDILT and LT-MEM.

**Step 4:** Calculate the estimated interval  $[b_L, b_U]$  for  $b$  using Eq. (17).

**Step 5:** Substitute the numerical ICLT  $\hat{\mathcal{L}}^I[f_Z(z);c]$  and RCLT  $\hat{\mathcal{L}}^R[f_Z(z);c]$  within the interval  $[b_L, b_U]$  into Eq. (16) to obtain the numerical PDF  $\hat{f}_Z(z)$ .

The NDILT method (Eq. (16)) enables accurate estimation of the main body of highly complex multi-modal PDFs, using a limited number of sample points, as demonstrated in the test examples in Section 5. On the other hand, the series with truncation errors and trigonometric terms in Eq. (16) may introduce oscillations and negative values in the tails of the estimated PDF  $\hat{f}_Z(z)$ . Thus, the NDILT method is preferred when the distribution tail is not a primary concern.

#### 4. LT-MEM for probability density estimation

This section proposes another PDF estimation method, i.e., LT-MEM, to address the oscillations and non-positivity in the tails of the NDILT method proposed in Section 3.2. The proposed LT-MEM leverages the values of RCLT as constraints of the maximum entropy principle, enabling effective reconstruction of probability distributions with complex shapes across the entire distribution range. Furthermore, the relationship between the RCLT and the integer moments is derived, revealing its ability to encapsulate substantial probabilistic information and thus highlighting its strengths in modelling complex distributions.

##### 4.1. Generalized paradigm of the MEM

The MEM is a well-established approach for recovering PDFs from a limited number of moments. This method guarantees that the recovered PDF remains unbiased and accurately reflects the available moments while minimizing the introduction of extraneous or misleading information [43,53].

In MEM, the Shannon entropy of  $f_Z(z)$  is given by

$$\mathcal{H}[f_Z(z)] = - \int_{-\infty}^{\infty} f_Z(z) \ln[f_Z(z)] dz. \tag{19}$$

Generally, the unified framework for various MEMs can be expressed as

$$\left\{ \begin{array}{l} \text{Find: } \hat{f}_Z(z) \\ \text{Maximize: } \mathcal{H}[\hat{f}_Z(z)] = -\int_{-\infty}^{\infty} \hat{f}_Z(z) \ln[\hat{f}_Z(z)] dz \\ \text{Subject to: } \int_{-\infty}^{\infty} \hat{f}_Z(z) dz = 1 \\ \int_{-\infty}^{\infty} (T(z))^{\alpha_l} \hat{f}_Z(z) dz = \hat{\mathcal{M}}_{T(Z)}^{\alpha_l}, \quad l = 1, 2, \dots, L \end{array} \right. , \tag{20}$$

where  $\hat{f}_Z(z)$  represents the estimated PDF obtained by the MEM;  $\hat{\mathcal{M}}_{T(Z)}^{\alpha_l}$  denotes the  $\alpha_l$ th order sample moment of  $T(Z)$ ;  $L$  indicates the total number of the statistical moments; and  $T(\cdot)$  is a user-defined mapping function. IM-MEM and FM-MEM correspond to integer and fractional values of  $\alpha_l$ , respectively.

As mentioned above, traditional MEMs, which rely on integer or fractional moments, often require large data samples and face challenges related to inflexibility and numerical instability. These issues make them difficult to apply to the estimation of complex PDFs commonly encountered in real-world engineering, thereby limiting their practical applicability [32,42]. On the other hand, while the proposed NDILT method can accurately and flexibly reconstruct complex PDFs in the main body, it may experience oscillations and non-positivity in the tails. To address these limitations, the so-called LT-MEM is proposed for output PDF estimation, which is described in detail in the following sections.

#### 4.2. Proposed LT-MEM

To uniformly address diverse problems and enhance the robustness of the proposed LT-MEM across various distribution domains, an intermediate random variable  $Y$  is introduced to normalize  $Z$ :

$$Y = (Z - \hat{\mu}_Z) / \hat{\sigma}_Z, \tag{21}$$

where  $\hat{\mu}_Z$  and  $\hat{\sigma}_Z$  denote the sample mean and standard deviation of  $Z$ , respectively.

The estimated mean  $\hat{\mu}_Z$  and standard deviation  $\hat{\sigma}_Z$  of  $Z$  can be obtained from the samples  $\bar{z}$  without requiring for additional evaluation of the  $G(\cdot)$  function, as shown below:

$$\hat{\mu}_Z = \frac{1}{n_t} \sum_{i=1}^{n_t} \bar{z}_i, \quad \hat{\sigma}_Z = \sqrt{\frac{1}{n_t - 1} \sum_{i=1}^{n_t} (\bar{z}_i - \hat{\mu}_Z)^2}. \tag{22}$$

Once the estimated PDF  $\hat{f}_Y(y)$  of  $Y$  is obtained, the estimated PDF  $\hat{f}_Z(z)$  of  $Z$  can be determined accordingly and is expressed as

$$\hat{f}_Z(z) = \hat{f}_Y(y) / \hat{\sigma}_Z. \tag{23}$$

Then, the focus shifts to deriving the PDF  $\hat{f}_Y(y)$ , which can be achieved using the proposed LT-MEM method.

In the LT-MEM, the RCLT of  $f_Y(y)$ , denoted as  $\mathcal{L}^R[f_Y(y); c]$ , is specified as the constraint in MEM. For clarity, the expression for the RCLT of  $f_Y(y)$  is restated as follows

$$\mathcal{L}^R[f_Y(y); c] = \mathbb{E}[\exp(-aY) \cos(-bY)] = \int_{\Omega_Y} f_Y(y) \exp(-ay) \cos(-by) dy, \tag{24}$$

where  $\Omega_Y$  is the sample space of  $Y$ .

To illustrate the mathematical properties of the RCLT,  $\mathcal{L}^R[f_Y(y); c]$ , of  $f_Y(y)$ , consider the Taylor series expansion of the term,  $\exp(-aY) \cos(-bY)$ , around the origin:

$$\begin{aligned} \exp(-aY) \cos(-bY) &= 1 - aY + \frac{(a^2 - b^2) Y^2}{2!} - \frac{(a^3 - 3ab^2) Y^3}{3!} + \dots \\ &+ \frac{(-1)^K}{K!} \sum_{k=0}^{\lfloor K/2 \rfloor} C(K, 2k) (-1)^k a^{n-2k} b^{2k} Y^K + \dots, \end{aligned} \tag{25}$$

where  $\lfloor \cdot \rfloor$  denotes the floor function; and  $C(K, 2k)$  is the binomial coefficient, which can be computed as follows

$$C(K, 2k) = \frac{K!}{(2k)! (K - 2k)!}. \tag{26}$$

Thus, the  $\mathcal{L}^R[f_Y(y); c]$  can be rewritten as

$$\begin{aligned} \mathcal{L}^R[f_Y(y); c] &= \mathbb{E}[\exp(-aY) \cos(-bY)] \\ &= 1 - a\mathbb{E}[Y] + \frac{(a^2 - b^2) \mathbb{E}[Y^2]}{2!} - \frac{(a^3 - 3ab^2) \mathbb{E}[Y^3]}{3!} + \dots \\ &+ \frac{(-1)^K}{K!} \sum_{k=0}^{\lfloor K/2 \rfloor} C(K, 2k) (-1)^k a^{n-2k} b^{2k} \mathbb{E}[Y^K] + \dots. \end{aligned} \tag{27}$$

Here,  $\mathcal{L}^R[f_Y(y); c]$  is expressed as a weighted summation of an infinite number of raw moments of  $Y$ , indicating that it encompasses a substantial amount of probabilistic information related to its raw moment counterpart.

Likewise, the expansion of  $\exp(-aY) \cos(-bY)$  can be also performed at the mean of  $Y$ , denoted as  $\mu_Y = \mathbb{E}[Y]$ , following the same pattern as the expansion around the origin (Eq. (25)). In this case, each derivative is evaluated at  $\mu_Y$ , resulting in a more complex expression due to the presence of  $\mu_Y$  in the exponential and trigonometric functions. For higher-order terms, the general pattern of the powers of  $a$  and  $b$  will persist, and the trigonometric and exponential factors will reflect the shift by  $\mu_Y$ . Thus, the expansion up to the infinite order will involve a series of increasingly complex terms comprising powers of  $(Y - \mu_Y)$ ,  $\exp(-a\mu_Y)$ , and trigonometric factors such as  $\cos(b\mu_Y)$  and  $\sin(b\mu_Y)$ . For simplicity, the expansion of  $\mathcal{L}^R [f_Y(y); c]$  at  $\mu_Y$  is presented with the first three explicit expressions as follows

$$\begin{aligned} \mathcal{L}^R [f_Y(y); c] &= \mathbb{E}(\exp(-aY) \cos(-bY)) \\ &= \frac{\cos(b\mu_Y)}{\exp(a\mu_Y)} - \frac{[a \cos(b\mu_Y) + b \sin(b\mu_Y)] \mathbb{E}[(Y - \mu_Y)]}{\exp(a\mu_Y)} \\ &\quad + \frac{[(a^2 - b^2) \cos(b\mu_Y) + 2ab \sin(b\mu_Y)] \mathbb{E}[(Y - \mu_Y)^2]}{2 \exp(a\mu_Y)} + \dots, \end{aligned} \tag{28}$$

where  $\mathbb{E}[(Y - \mu_Y)^K]$  is the  $K$ th central moment of  $Y$ .

Eqs. (27) and (28) clearly indicate that the  $\mathcal{L}^R [f_Y(y); c]$  encapsulates the statistical information about moments. This suggests that the potential utility of  $\mathcal{L}^R [f_Y(y); c]$  for estimating unknown PDFs is significant, as it can capture a wealth of probabilistic information even for small values of  $a$  and  $b$ . However, despite its conceptual advantages, directly calculating  $\mathcal{L}^R [f_Y(y); c]$  using Eq. (24) is often challenging or even infeasible, given that  $f_Y(y)$  is unknown. Consequently, numerical approximations of  $\mathcal{L}^R [f_Y(y); c]$  become essential, which can be calculated using methods analogous to those in Eq. (14), and can be expressed as

$$\hat{\mathcal{L}}^R [f_Y(y); c] = \frac{1}{n_t} \sum_{i=1}^{n_t} \exp(-a\bar{y}_i) \cos(-b\bar{y}_i), \tag{29}$$

where the samples of  $Y$ , denoted as  $\bar{\mathbf{y}} = (\bar{y}_1, \bar{y}_2, \dots, \bar{y}_i, \dots, \bar{y}_{n_t})$ , can be calculated using Eq. (21) based on the samples  $\bar{\mathbf{z}}$ .

Here, by treating the numerical RCLT of  $f_Z(z)$ , i.e.,  $\hat{\mathcal{L}}^R [f_Y(y); c]$ , as constraints within the entropy maximum problem presented in Eq. (20), the proposed LT-MEM can be readily formulated as follows

$$\left\{ \begin{array}{l} \text{Find: } \hat{f}_Y(y) \\ \text{Maximize: } \mathcal{H}[\hat{f}_Y(y)] = -\int_{\Omega_Y} \hat{f}_Y(y) \ln[\hat{f}_Y(y)] dy \\ \text{Subject to: } \int_{\Omega_Y} \hat{f}_Y(y) dy = 1 \\ \int_{\Omega_Y} \hat{f}_Y(y) \exp(-a_l y) \cos(-b_l y) dy = \hat{\mathcal{L}}_l^R [f_Y(y); a_l, b_l], \quad l = 1, 2, \dots, L \end{array} \right. , \tag{30}$$

where  $\hat{\mathcal{L}}_l^R [f_Y(y); a_l, b_l]$  is the  $l$ th numerical RCLT of  $f_Y(y)$  with  $a = a_l$  and  $b = b_l$ ;  $L$  stands for the number of the given RCLT constraints;  $\hat{f}_Y(y)$  is the estimation PDF; and  $\mathbf{a} = [a_1, \dots, a_L]$  and  $\mathbf{b} = [b_1, \dots, b_L]$  are undetermined parameters.

The numerical RCLT constraints introduced in Eq. (30) incorporate bounded trigonometric terms alongside the FEMs [29,35,43]. This enhancement not only preserves the benefits of FEMs but also increases the flexibility of the MEM. As a result, the proposed LT-MEM can reconstruct more complex probability distributions without compromising the stability of the optimization process. Moreover, by employing the values of RCLT as constraints instead of relying solely on integer or fractional moments, the traditional MEM is effectively extended without introducing theoretical challenges.

The Lagrangian function associated with Eq. (30) can then be formulated as follows [29,34]

$$\begin{aligned} \mathcal{L} &= -\int_{\Omega_Y} \hat{f}_Y(y) \ln[\hat{f}_Y(y)] dy - (\lambda_0 - 1) \left[ \int_{\Omega_Y} \hat{f}_Y(y) dy - 1 \right] \\ &\quad - \sum_{l=1}^L \lambda_l \left[ \int_{\Omega_Y} \hat{f}_Y(y) \exp(-a_l y) \cos(-b_l y) dy - \hat{\mathcal{L}}_l^R [f_Y(y); a_l, b_l] \right], \end{aligned} \tag{31}$$

where  $\lambda = [\lambda_1, \lambda_2, \dots, \lambda_l, \dots, \lambda_L]$  denotes the Lagrange multiplier vector.

To obtain the optimal solution of Eq. (30), the following condition must be satisfied

$$\begin{aligned} \frac{\partial \mathcal{L}}{\partial \hat{f}_Y(y)} &= \delta \mathcal{L} \\ &= -\delta \int_{\Omega_Y} \hat{f}_Y(y) \ln[\hat{f}_Y(y)] dy - (\lambda_0 - 1) \delta \left[ \int_{\Omega_Y} \hat{f}_Y(y) dy - 1 \right] \\ &\quad - \sum_{l=1}^L \lambda_l \delta \left[ \int_{\Omega_Y} \hat{f}_Y(y) \exp(-a_l y) \cos(-b_l y) dy - \hat{\mathcal{L}}_l^R [f_Y(y); a_l, b_l] \right] \\ &= -\int_{\Omega_Y} \{ \delta \hat{f}_Y(y) \ln[\hat{f}_Y(y)] + \hat{f}_Y(y) \delta \{ \ln[\hat{f}_Y(y)] \} \} dy \end{aligned}$$

$$\begin{aligned}
 & -(\lambda_0 - 1) \left[ \int_{\Omega_Y} \delta \hat{f}_Y(y) dy \right] - \sum_{l=1}^L \lambda_l \int_{\Omega_Y} \delta \hat{f}_Y(y) \exp(-a_l y) \cos(-b_l y) dy \\
 & = - \int_{\Omega_Y} \left\{ \ln [\hat{f}_Y(y)] + \hat{f}_Y(y) \frac{1}{\hat{f}_Y(y)} \right\} \delta \hat{f}_Y(y) dy \\
 & - \int_{\Omega_Y} (\lambda_0 - 1) \delta \hat{f}_Y(y) dy - \int_{\Omega_Y} \sum_{l=1}^L \lambda_l \exp(-a_l y) \cos(-b_l y) \delta \hat{f}_Y(y) dy \\
 & = \int_{\Omega_Y} \left\{ -\ln [\hat{f}_Y(y)] - 1 - (\lambda_0 - 1) - \sum_{l=1}^L \lambda_l \exp(-a_l y) \cos(-b_l y) \right\} \delta \hat{f}_Y(y) dy \\
 & = 0.
 \end{aligned} \tag{32}$$

So that

$$-\ln [\hat{f}_Y(y)] - 1 - (\lambda_0 - 1) - \sum_{l=1}^L \lambda_l \exp(-a_l y) \cos(-b_l y) = 0, \tag{33}$$

which yields the analytical expression of  $\hat{f}_Y(y)$  as follows

$$\hat{f}_Y(y) = \exp \left[ -\lambda_0 - \sum_{l=1}^L \lambda_l \exp(-a_l y) \cos(-b_l y) \right]. \tag{34}$$

Considering the normalization condition of the PDF, we have

$$\begin{aligned}
 \int \hat{f}_Y(y) dy & = \int_{\Omega_Y} \exp \left[ -\lambda_0 - \sum_{l=1}^L \lambda_l \exp(-a_l y) \cos(-b_l y) \right] dy \\
 & = \frac{1}{\exp(\lambda_0)} \int_{\Omega_Y} \exp \left[ -\sum_{l=1}^L \lambda_l \exp(-a_l y) \cos(-b_l y) \right] dy \\
 & = 1.
 \end{aligned} \tag{35}$$

Then, the coefficient  $\lambda_0$  can be determined accordingly as follows

$$\lambda_0 = \ln \left\{ \int_{\Omega_Y} \exp \left[ -\sum_{l=1}^L \lambda_l \exp(-a_l y) \cos(-b_l y) \right] dy \right\}. \tag{36}$$

The maximum entropy problem (Eq. (30)) can be solved by reformulating it as an equivalent dual problem, which involves minimizing Kullback–Leibler divergence [54] between the true PDF  $f_Y(y)$  and its estimation  $\hat{f}_Y(y)$  [34,55]. The Kullback–Leibler divergence is defined as follows

$$\begin{aligned}
 \mathcal{K}[f, \hat{f}] & = \int_{\Omega_Y} f_Y(y) \ln [f_Y(y) / \hat{f}_Y(y)] dy \\
 & = \int_{\Omega_Y} f_Y(y) \ln [f_Y(y)] dy - \int_{\Omega_Y} f_Y(y) \ln [\hat{f}_Y(y)] dy.
 \end{aligned} \tag{37}$$

Generally, a smaller Kullback–Leibler divergence indicates a smaller difference between the true PDF and its approximation, suggesting higher estimation accuracy.

Substituting Eqs. (19) and (34) into Eq. (37) yields

$$\begin{aligned}
 \mathcal{K}[f, \hat{f}] & = -\mathcal{H}[f_Y(y)] - \int_{\Omega_Y} \left[ -\lambda_0 - \sum_{l=1}^L \lambda_l \exp(-a_l y) \cos(-b_l y) \right] f_Y(y) dy \\
 & = -\mathcal{H}[f_Y(y)] + \lambda_0 + \sum_{l=1}^L \lambda_l \int_{\Omega_Y} \exp(-a_l y) \cos(-b_l y) f_Y(y) dy \\
 & = -\mathcal{H}[f_Y(y)] + \lambda_0 + \sum_{l=1}^L \lambda_l \hat{\mathcal{L}}_l^R[f_Y(y); a_l, b_l],
 \end{aligned} \tag{38}$$

where the entropy  $-\mathcal{H}[f_Y(y)]$  of the true PDF is constant and independent of  $\hat{\mathcal{L}}_l^R[f_Y(y); a_l, b_l]$  and  $\lambda = [\lambda_1, \lambda_2, \dots, \lambda_L]$ .

Therefore, one can define

$$\begin{aligned}
 \mathcal{W}(\mathbf{a}, \mathbf{b}, \lambda) & = \mathcal{K}[f, \hat{f}] + \mathcal{H}[f_Y(y)] \\
 & = \lambda_0 + \sum_{l=1}^L \lambda_l \hat{\mathcal{L}}_l^R[f_Y(y); a_l, b_l].
 \end{aligned} \tag{39}$$

In this context, the constrained optimization problem in Eq. (30) can be reformulated into an unconstrained form as follows

$$\begin{cases} \text{Find: } \mathbf{a} = [a_1, \dots, a_L], \mathbf{b} = [b_1, \dots, b_L] \text{ and } \lambda = [\lambda_1, \dots, \lambda_L] \\ \text{Minimize: } \mathcal{W}(\mathbf{a}, \mathbf{b}, \lambda) = \lambda_0 + \sum_{l=0}^L \lambda_l \hat{\mathcal{L}}_l^R [f_Y(y); a_l, b_l] \end{cases} \quad (40)$$

The LT-MEM not only effectively reconstructs complex-shaped probability distributions but also eliminates the tail oscillations observed in NDILT, ensuring the non-negativity and normalization condition of the estimated PDF. Eq. (40) can be performed using the simplex search method in Matlab [34]. Subsequently, the parameter  $\mathbf{a}$ ,  $\mathbf{b}$  and the Lagrange multipliers  $\lambda$  can be determined accordingly. Finally, the estimated PDF  $\hat{f}_Y(y)$  of  $Y$  is calculated by substituting the optimized values of  $\mathbf{a}$ ,  $\mathbf{b}$  and  $\lambda$ , into Eqs. (34) and (36). The PDF  $f_Z(z)$  is then obtained using Eq. (23).

### 4.3. Parameters configuration in LT-MEM

It is important to note that several parameters in the LT-MEM need to be preconfigured before solving the optimization problem (Eq. (40)). These parameters include the estimated optimization bounds for  $\mathbf{a}$ ,  $\mathbf{b}$ , and  $\lambda$ , denoted as  $[\hat{a}_L, \hat{a}_U]$ ,  $[\hat{b}_L, \hat{b}_U]$  and  $[\hat{\lambda}_L, \hat{\lambda}_U]$ , respectively. Additionally, the number of constraints  $L$ , the approximate integration limits  $[\hat{y}_L, \hat{y}_U]$  for the estimated PDF  $\hat{f}_Y(y)$ , and the number of sample points  $n_l$ , also need to be specified. In this paper, the values for these parameters are determined empirically, as detailed below.

To approximate the integration limits  $[\hat{y}_L, \hat{y}_U]$  of  $\hat{f}_Y(y)$ , a methodology based on the available set of moments is introduced [56, 57]. In this approach, the original moments  $m_J$  of  $Y$ , for  $J = 0, 1, \dots, J$ , are first shifted to point-of-interest  $C$  using the following linear transformation [56]:

$$\hat{m}_J = \sum_{j=0}^J (C(J, j) (-C)^{J-j} m_j), \quad (41)$$

where  $\hat{m}_J$  represents the linearly shifted moment.

Then, determine the maximal mass  $\tau$  at 0, such that [56]

$$\tau = \begin{vmatrix} \hat{m}_0 & \hat{m}_1 & \dots & \hat{m}_J \\ \hat{m}_1 & \hat{m}_2 & \dots & \hat{m}_{J+1} \\ \vdots & \vdots & \ddots & \vdots \\ \hat{m}_J & \hat{m}_{J+1} & \dots & \hat{m}_{2J} \end{vmatrix} \cdot \begin{vmatrix} \hat{m}_2 & \hat{m}_3 & \dots & \hat{m}_{J+1} \\ \hat{m}_3 & \hat{m}_4 & \dots & \hat{m}_{J+2} \\ \vdots & \vdots & \ddots & \vdots \\ \hat{m}_{J+1} & \hat{m}_{J+2} & \dots & \hat{m}_{2J} \end{vmatrix}^{-1}, \quad (42)$$

where  $\hat{J} = \lfloor \frac{J}{2} \rfloor$ ; and the  $\tau$  is specified as  $\tau = 10^{-(\hat{J}+1)}$ . Then, the Eq. (42) is solved in real coordinate space for  $C$  [56], with the solutions serving as the approximate lower and upper integration limits, i.e.,  $[\hat{y}_L, \hat{y}_U]$ . It is recommended that the number  $J$  of original moments  $m_J$  be between 4 and 8 [56]; in this paper,  $J = 4$  is adopted.

The estimated optimization interval  $[\hat{b}_L, \hat{b}_U]$  of  $b$  needs to be specified in a manner similar to Eq. (17), with a slight variation. Since the variable  $Y$  is a normalized intermediate variable, the maximum value of RCLT with  $b = 0$ , i.e.,  $\mathcal{L}^R [f_Z(z); a, 0]$ , is typically close to 1 across different problems. Therefore, the estimated optimization interval  $[\hat{b}_L, \hat{b}_U]$  for  $b$  in LT-MEM, where  $\hat{b}_L = -\hat{b}_U$ , is determined by satisfying the following condition:

$$\underline{b}_U \leq \hat{b}_U \leq \overline{b}_U, \quad (43)$$

where

$$\begin{cases} \overline{b}_U = \min \left\{ \hat{b} \mid \forall b \in (\hat{b}, +\infty), \left| \hat{\mathcal{L}}^R (f_Z(z); a, b) \right| \leq \rho_1 \right\}, \hat{b} \in [0, +\infty) \\ \underline{b}_U = \min \left\{ \hat{b} \mid \forall b \in (\hat{b}, +\infty), \left| \hat{\mathcal{L}}^R (f_Z(z); a, b) \right| \leq \rho_2 \right\}, \hat{b} \in [0, +\infty) \end{cases}, \quad (44)$$

in which  $a$  is specified as  $-0.01$ .

In this paper, the number  $n_l$  of points in the representative point set  $\mathcal{P}_\theta$  used for calculating the samples of  $Z$  is set as follows:  $n_l = 400$  for estimating simple standard distribution (e.g., normal, gamma, lognormal, etc.),  $n_l = 1000$  for low-dimensional problems ( $d \leq 20$ ),  $n_l = 1500$  or more as appropriate for high-dimensional problems ( $d > 20$ ). The number  $L$  of constraints for the numerical RCLT  $\hat{\mathcal{L}}_l^R [f_Y(y); a_l, b_l]$  in the LT-MEM is recommended to be between 3 and 10, depending on the complexity of the distribution. In this study,  $L = 3$  is chosen for uni-modal probability distributions and  $L = 6$  for multi-modal cases. The estimated optimization bounds  $[\hat{\lambda}_L, \hat{\lambda}_U]$  for the Lagrange multiplier  $\lambda$  are suggested to range from  $[\hat{\lambda}_L, \hat{\lambda}_U] = [-50, 50]$  to  $[\hat{\lambda}_L, \hat{\lambda}_U] = [-100, 100]$ . In this study,  $[\hat{\lambda}_L, \hat{\lambda}_U] = [-50, 50]$  is selected. For the optimization parameter  $\mathbf{a}$ , the suggested optimization bounds  $[\hat{a}_L, \hat{a}_U]$  range from  $[\hat{a}_L, \hat{a}_U] = [-0.1, 0.1]$  to  $[\hat{a}_L, \hat{a}_U] = [-10, 10]$ , which should be chosen carefully based on the specific problem at hand. In this study, an enumeration strategy is employed to determine the final optimization bound  $[\hat{a}_L, \hat{a}_U]$ . In this process, the LT-MEM is solved sequentially for each optimization bound  $[\hat{a}_L, \hat{a}_U] = [-\bar{i}\Delta_a, \bar{i}\Delta_a]$ , where  $\bar{i} = 1, 2, \dots, 100$ , and a step size of  $\Delta_a = 0.1$  is adopted. Then, the bound that yields the steady-state optimal solution of the objective function  $\mathcal{W}(\mathbf{a}, \mathbf{b}, \lambda)$  is selected from the interval  $[-\bar{i}\Delta_a, \bar{i}\Delta_a]$  as the final optimization bounds  $[\hat{a}_L, \hat{a}_U]$ .

Finally, the optimization problem in Eq. (40) is reformulated as a bounded optimization problem, represented as follows:

$$\begin{cases} \text{Find: } \mathbf{a} = [a_1, \dots, a_L], \mathbf{b} = [b_1, \dots, b_L] \text{ and } \lambda = [\lambda_1, \dots, \lambda_L] \\ \text{Minimize: } \mathcal{W}(\mathbf{a}, \mathbf{b}, \lambda) = \lambda_0 + \sum_{l=0}^L \lambda_l \hat{\mathcal{L}}_l^R [f_Y(y); a_l, b_l] \\ \text{Subject to: } \hat{a}_L \leq a_l \leq \hat{a}_U, \hat{b}_L \leq b_l \leq \hat{b}_U, \hat{\lambda}_L \leq \lambda_l \leq \hat{\lambda}_U, l = 1, 2, \dots, L \end{cases} \quad (45)$$

**Table 1**  
Distribution information for Example 1.

Distribution	Exact PDF	$\kappa$	$\gamma$	Weights $\omega$
Normal	$f(z; \kappa, \gamma) = \frac{1}{\sqrt{2\pi\gamma^2}} \exp\left(-\frac{(z-\kappa)^2}{2\gamma^2}\right), z \in \mathbb{R}.$	0	1	1
Lognormal	$f(z; \kappa, \gamma) = \frac{1}{z\gamma\sqrt{2\pi}} \exp\left\{-\frac{(\log z - \kappa)^2}{2\gamma^2}\right\}, z > 0.$	-0.0196	0.1980	1
Gamma	$f(z; \kappa, \gamma) = \frac{1}{\Gamma(\kappa)\gamma^\kappa} z^{\kappa-1} \exp(-z/\gamma), z > 0.$	9.5000	0.5000	1
Exponential	$f(z; \kappa) = \frac{1}{\kappa} \exp\left(-\frac{z}{\kappa}\right), z \geq 0.$	0.6667	-	1
Gaussian mixture	$f(z; \kappa_1, \kappa_2, \gamma_1, \gamma_2, \omega_1, \omega_2) = \sum_{i=1}^2 \omega_i \frac{1}{\sqrt{2\pi\gamma_i^2}} \exp\left(-\frac{(z-\kappa_i)^2}{2\gamma_i^2}\right), z \in \mathbb{R}.$	[1, 10]	[0.75, 1]	[0.5, 0.5]
Gaussian mixture	$f(z; \kappa_1 \sim \kappa_3, \gamma_1 \sim \gamma_3, \omega_1 \sim \omega_3) = \sum_{i=1}^3 \omega_i \frac{1}{\sqrt{2\pi\gamma_i^2}} \exp\left(-\frac{(z-\kappa_i)^2}{2\gamma_i^2}\right), z \in \mathbb{R}.$	[10, 15, 20]	[1, 1, 1]	[0.3, 0.4, 0.3]

Note:  $\Gamma(\cdot)$  = gamma function.

#### 4.4. Step-by-step procedure of the proposed LT-MEM method

The calculation procedure of the proposed LT-MEM is illustrated in Fig. 3, with the detailed steps outlined below:

**Step 1:** Same as **Step 1:** of the NDILT method outlined in Section 3.3.

**Step 2:** Same as **Step 2:** of the NDILT method (see Section 3.3).

**Step 3:** Calculate the samples  $\bar{y} = (\bar{y}_1, \bar{y}_2, \dots, \bar{y}_i, \dots, \bar{y}_{n_i})$  of the intermediate random variable  $Y$  using Eq. (21).

**Step 4:** Approximate the integration limit  $[\hat{y}_L, \hat{y}_U]$  of  $\hat{f}_Y(y)$  by solving Eq. (42).

**Step 5:** Determine the estimated optimization bounds for  $\mathbf{a}$ ,  $\mathbf{b}$ , and  $\lambda$ , i.e.,  $[\hat{a}_L, \hat{a}_U]$ ,  $[\hat{b}_L, \hat{b}_U]$  and  $[\hat{\lambda}_L, \hat{\lambda}_U]$ , respectively, as well as the number  $L$  of constraints, following the guidelines provided in Section 4.3.

**Step 6:** Solve the optimization problem expressed in Eq. (45) using the bounded simplex search method in MATLAB to obtain the optimized parameters of  $\mathbf{a}$ ,  $\mathbf{b}$ , and  $\lambda$ . In each iteration, the constrains  $\hat{L}_l^R [f_Y(y); a_l, b_l]$  are calculate using Eq. (29), and  $\lambda_0$  is determined using Eq. (36).

**Step 7:** Substitute the optimized parameters of  $\mathbf{a}$ ,  $\mathbf{b}$ , and  $\lambda$  into Eq. (34) to calculate the estimation PDF  $\hat{f}_Y(y)$ .

**Step 8:** Calculate the estimated PDF  $\hat{f}_Z(z)$  using Eq. (23).

### 5. Numerical examples

This section presents four examples, encompassing both analytical and numerical cases, to demonstrate the performance of the proposed NDILT method and LT-MEM for PDF estimation. For comparison, the crude MCS and the FEM-MEM [29,35,43] are also employed across all examples. Note that the FEM-MEM utilizes NGV-NTM as in the proposed methods.

#### 5.1. Example 1: Analytical distributions

To validate the proposed method, several analytical uni-modal and multi-modal distributions with known exact PDFs are considered. Details are summarized in Table 1.

The NDILT and LT-MEM methods are implemented to reconstruct the PDFs listed in Table 1 using 400 samples. Results, including PDFs, Cumulative Distribution Functions (CDF) and Probability Of Exceedance (POE) curves, are shown in Figs. 4, 5, 6, 7, 8 and 9, alongside crude MCS (with  $1 \times 10^7$  runs) and the FEM-MEM (with 400 runs) results. The LT-MEM parameter configurations are provided in Table 2. The results demonstrate that the proposed LT-MEM accurately reconstructs PDFs with pronounced skewness and heavy tails. In contrast, FEM-MEM performs well for distributions with minimal skewness and lighter tails, such as the standard normal distribution (see Fig. 4), but loses accuracy in the tails for heavily skewed distributions (see Figs. 5, 6 and 7). Additionally, LT-MEM effectively reconstructs both uni-modal and multi-modal distributions, whereas FEM-MEM encounters challenges with multi-modal cases (see Fig. 8). The NDILT algorithm also demonstrates flexibility and accuracy in reconstructing the main body of complex probability distributions, particularly for multi-modal forms (see Figs. 8 and 9). To further investigate the performance of the proposed methods in handling probability distributions with an exceptionally large number of modes, two Gaussian mixture models with 10 and 100 components are analysed, respectively. The results are shown in Figs. 10 and 11. It is observed that the NDILT method consistently achieves high accuracy in reconstructing the main body of probability distributions with tens of modes. On the other hand, the LT-MEM method is capable of accurately reconstructing distributions with a few modes across the entire domain, but may experience a reduction in accuracy and flexibility in the main body when applied to distributions with an exceptionally large number of modes. Additionally, while NDILT may exhibit oscillations and non-positivity in the tails, it remains competitive for applications focused on accurately capturing the main body of the probability distribution, where tail details are less critical. On the other hand, in scenarios requiring high precision in the tails, such as reliability assessments of systems with small failure probabilities (e.g.,  $< 10^{-4}$ ), the NDILT method may exhibit limited accuracy.

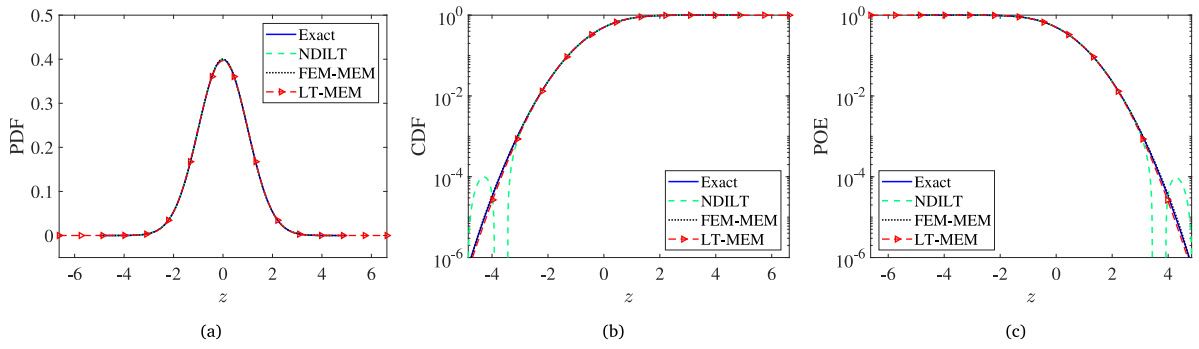


Fig. 4. (a) PDF, (b) CDF and (c) POE of Normal distribution in Example 1.

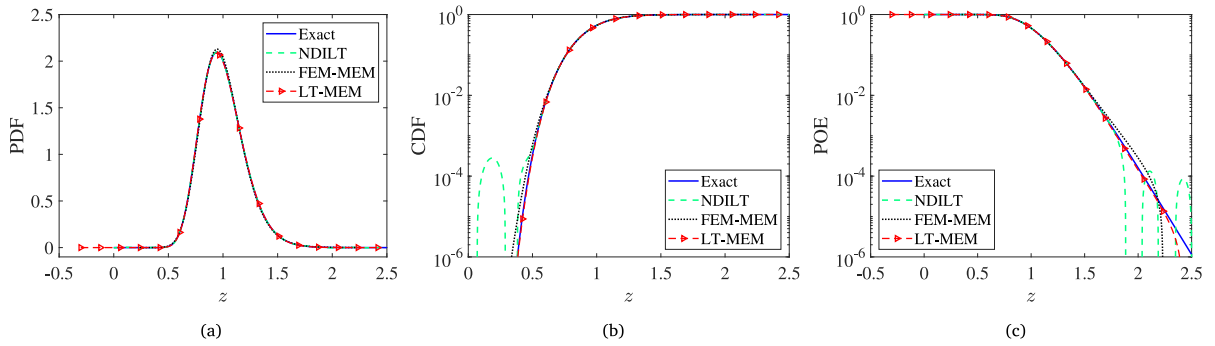


Fig. 5. (a) PDF, (b) CDF and (c) POE of Lognormal distribution in Example 1.

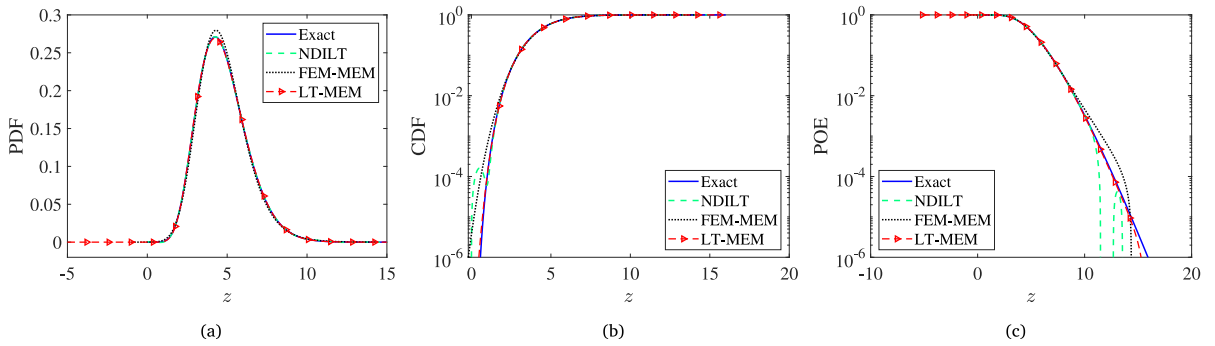


Fig. 6. (a) PDF, (b) CDF and (c) POE of gamma distribution in Example 1.

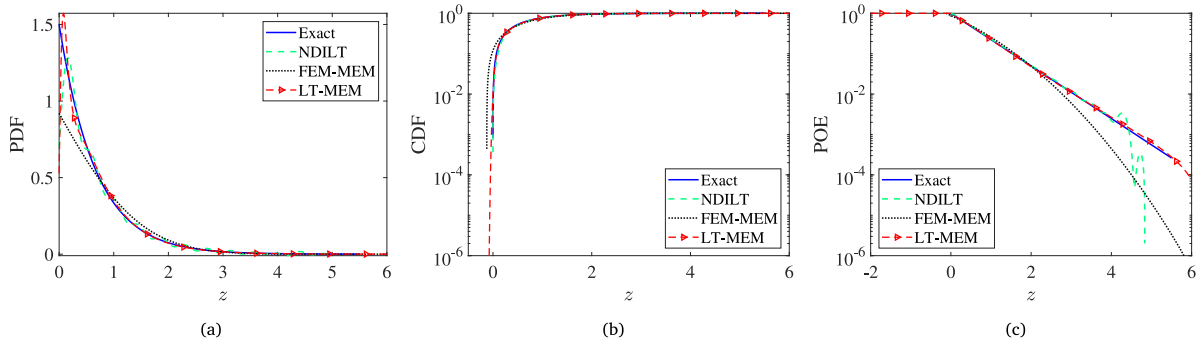


Fig. 7. (a) PDF, (b) CDF and (c) POE of exponential distribution in Example 1.

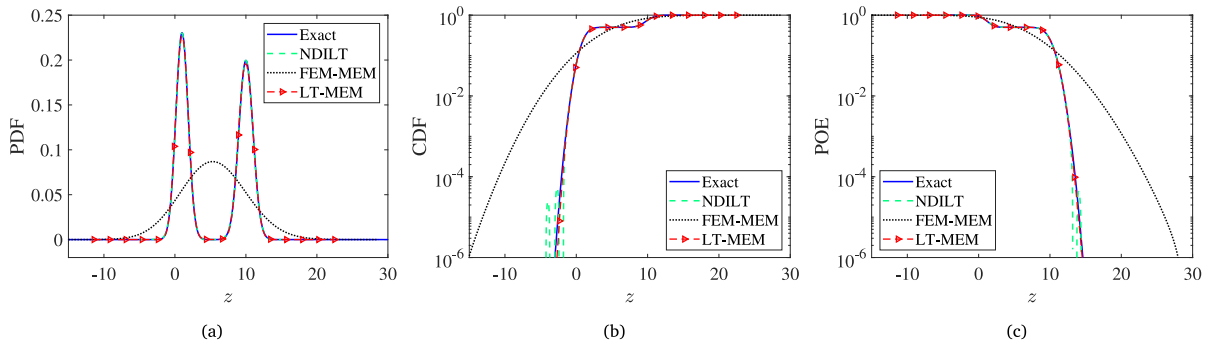


Fig. 8. (a) PDF, (b) CDF and (c) POE of Gaussian mixture distribution (2 components) in Example 1.

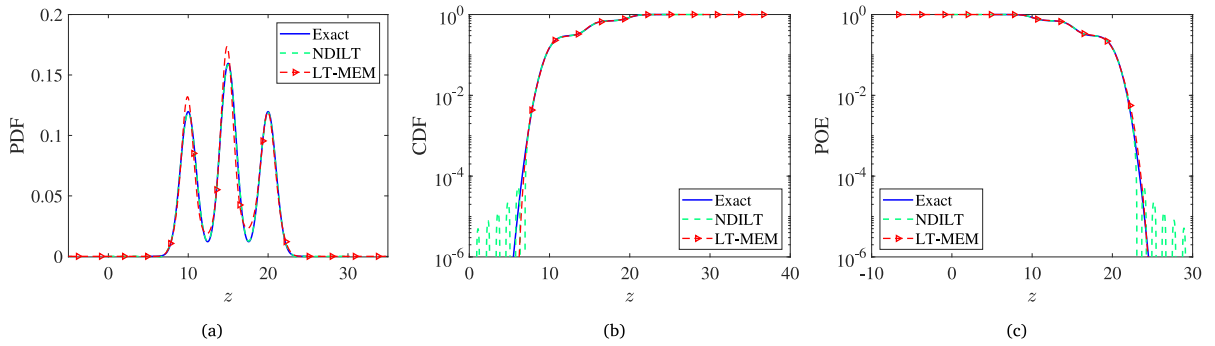


Fig. 9. (a) PDF, (b) CDF and (c) POE of Gaussian mixture distribution (3 components) in Example 1.

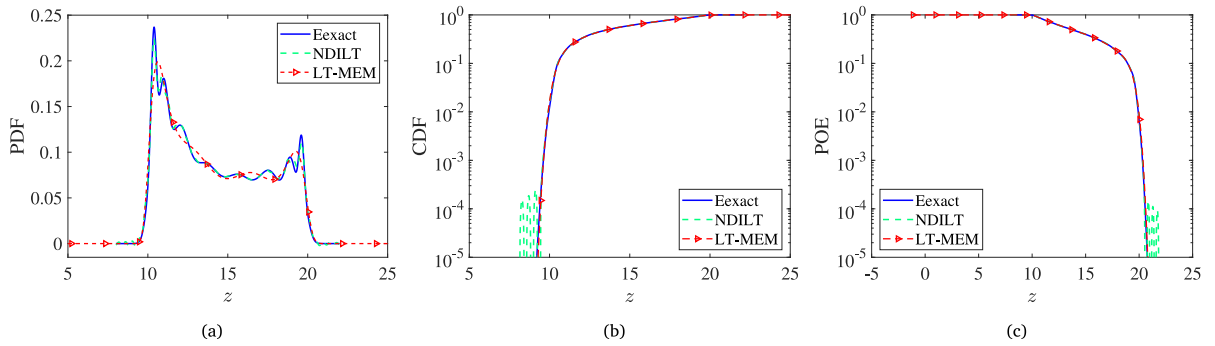


Fig. 10. (a) PDF, (b) CDF and (c) POE of Gaussian mixture distribution (10 components) in Example 1.

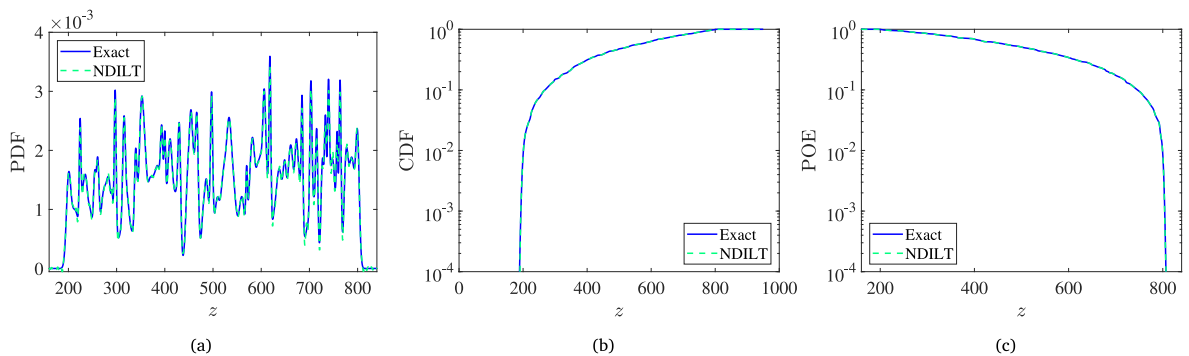


Fig. 11. (a) PDF, (b) CDF and (c) POE of Gaussian mixture distribution (100 components) in Example 1.

**Table 2**  
Parameters configuration of LT-MEM for Example 1.

Distribution	Optimization bounds			Parameter	
	$[\hat{\lambda}_L, \hat{\lambda}_U]$	$[\hat{a}_L, \hat{a}_U]$	$[\hat{b}_L, \hat{b}_U]$	$L$	$J$
Normal		[-4, 4]			
Lognormal		[-1.4, 1.4]			
Gamma		[-4, 4]	[-5, 5]	3	
Exponential	[-50, 50]	[-9.5, 9.5]			4
Gaussian mixture (2 components)		[-1.8, 1.8]		6	
Gaussian mixture (3 components)		[-0.5, 0.5]	[-15, 15]		

**Table 3**  
Basic random variables for Example 2.

Variable	Mean	Standard deviation	Weights $\omega$
$\Theta_1$	[6.0055, 6.9591, 10.4848, 14.4320]	[0.3838, 0.6509, 1.7566, 1.3628]	[0.2150, 0.1917, 0.4447, 0.1486]
$\Theta_2$	[7.5828, 9.8110, 14.6230, 17.5797]	[0.7462, 1.3062, 1.7064, 0.7076]	[0.1324, 0.3600, 0.2915, 0.2161]

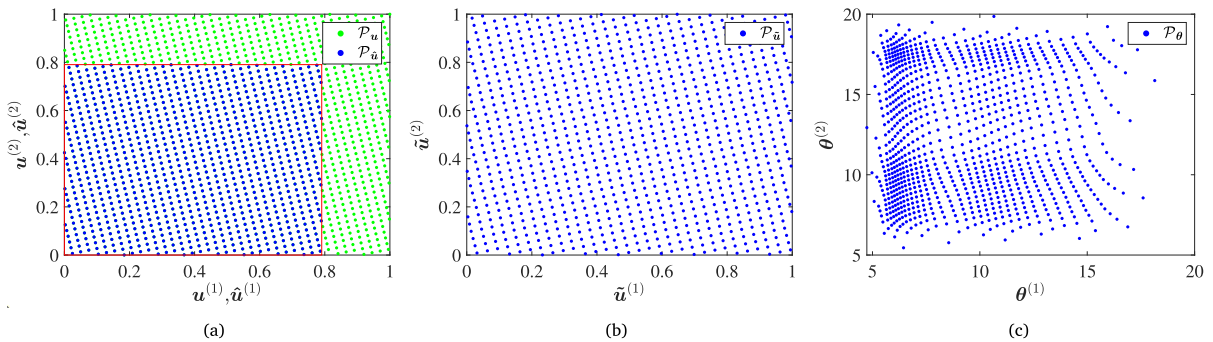


**Fig. 12.** Points in the first two-dimension (Example 2).

5.2. Example 2: A nonlinear mathematical model

In this example, a nonlinear mathematical model is considered, defined by the following response function [22,39]:

$$Z = 43 - \frac{360}{(\Theta_1 + 6)} + 0.02 (\Theta_2 - 14)^3, \tag{46}$$

where  $\Theta_1$  and  $\Theta_2$  are independent random variables, each following a multi-modal distribution modelled by a Gaussian mixture model. The parameters for these distributions are detailed in Table 3.

First, the representative point set  $\mathcal{P}_\theta$ , containing  $n_t = 1000$  points is generated using the NGV-NTM method (Appendix A). Fig. 12(a) shows the initial two-dimensional NTM point set  $\mathcal{P}_u$  (1597 points) and the two-dimensional cutting point set  $\mathcal{P}_{\hat{u}}$  (1000 points). The new generating vector  $\mathbf{v}$  is then derived from  $\mathcal{P}_{\hat{u}}$  using Two-Round Sorting Strategy (TRSS) (Eqs. (A.2) and (A.3)). Subsequently, the NGV-NTM point set  $\mathcal{P}_{\hat{u}}$  (1000 points) and representative point set  $\mathcal{P}_\theta$  (1000 points) are generated using Eqs. (A.4) and (A.5), as shown in Figs. 12(b) and 12(c), respectively.

The probability distribution of  $Z$  (Eq. (46)) is then estimated using the proposed NDILT algorithm and LT-MEM, based on output samples  $\bar{\mathbf{z}} = (\bar{z}_1, \bar{z}_2, \dots, \bar{z}_i, \dots, \bar{z}_{n_t})$ ,  $i = 1, 2, \dots, n_t$ , generated from 1000 evaluations of the response function. The LT-MEM parameters are configured as follows:  $[\hat{a}_L, \hat{a}_U] = [-0.8, 0.8]$ ,  $[\hat{b}_L, \hat{b}_U] = [-10, -10]$ ,  $[\hat{\lambda}_L, \hat{\lambda}_U] = [-50, -50]$ ,  $L = 6$  and  $J = 4$ . Fig. 13 presents the PDF curves calculated by the proposed methods and FEM-MEM with 1000 samples, with the MCS histogram (with  $1 \times 10^7$  runs) as reference. The PDF curves from the proposed methods show a good alignment with the reference histogram, whereas FEM-MEM exhibits significant deviations. The proposed methods accurately capture both the peaks and the valley of the bi-modal distribution, highlighting their effectiveness. Fig. 14 further displays the CDF and POE curves on a logarithmic scale, showing that the LT-MEM provides more accurate tail estimation compared to the NDILT algorithm, both with 1000 samples. The CDF curve generated by FEM-MEM deviates significantly from the MCS reference, highlighting its limitations in complex PDF estimation. Overall, LT-MEM captures the full bi-modal distribution range, especially the tails, while NDILT flexibly reconstructs the main body, with some tail oscillations. Quantitatively, the Kullback–Leibler divergence between LT-MEM and the MCS benchmark is 0.0013, demonstrating LT-MEM’s superior accuracy in reconstructing the multi-modal distribution across the entire distribution domain.

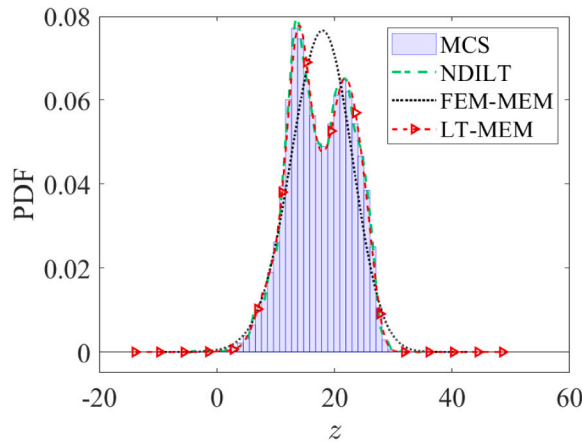


Fig. 13. PDF of Z in Example 2.

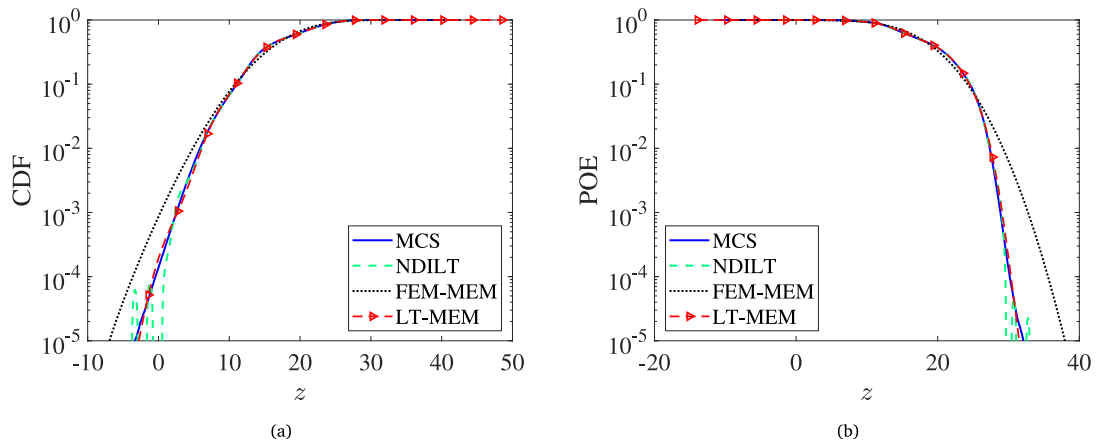


Fig. 14. (a) CDF and (b) POE of Z in Example 2.

Table 4  
Basic random variables for Example 3.

Variable	Description	Distribution	Mean	C.O.V	Weights $\omega$
$A$	Cross-sectional area	Normal	2000 mm <sup>2</sup>	0.20	1
$E$	Young's modulus	Normal	200 GPa	0.20	1
$P_0$	Vertical load	Gaussian mixture	[350, 700] kN	[0.1, 0.1]	[0.4, 0.6]
$P_1 \sim P_{12}$	Vertical loads	Lognormal	60 kN	0.20	1

Note: C.O.V = Coefficient of variation.

### 5.3. Example 3: A spatial truss structure

The third example considers a 120-bar spatial truss structure subjected to vertical loads, as shown in Fig. 15 [58–60]. The finite element model of this structure, built in OpenSEES software (Version: 3.2.2-x64), contains 49 nodes and 120 truss members. All members share the same cross-sectional area and Young's modulus, denoted by  $A$  and  $E$ , respectively. Vertical loads, labelled  $P_0 \sim P_{12}$ , are applied to nodes 0 ~ 12, respectively. This example focuses on the vertical displacement of node 0, denoted as  $Z$  ( $A, E, P_0 \sim P_{12}$ ), with  $A, E, P_0 \sim P_{12}$  treated as 15 random variables, as listed in Table 4.

A total of 1000 deterministic model analyses are conducted for this structure using the 1000 representative points in  $\mathcal{P}_\theta$ . The LT-MEM parameters are configured as follows:  $[\hat{a}_L, \hat{a}_U] = [-5.2, 5.2]$ ,  $[\hat{b}_L, \hat{b}_U] = [-10, -10]$ ,  $[\hat{\lambda}_L, \hat{\lambda}_U] = [-50, -50]$ ,  $L = 6$  and  $\mathcal{J} = 4$ . Figs. 16 and 17 present the PDFs, CDFs, and POEs for  $Z$ , as calculated by the proposed methods and MCS, with FEM-MEM results for comparison. For this multi-modal distribution, LT-MEM consistently provides highly accurate results, while NDILT captures the main body of the PDF effectively. The Kullback–Leibler divergence between LT-MEM and MCS results is 0.0012, highlighting LT-MEM's robustness and accuracy for PDF estimation.

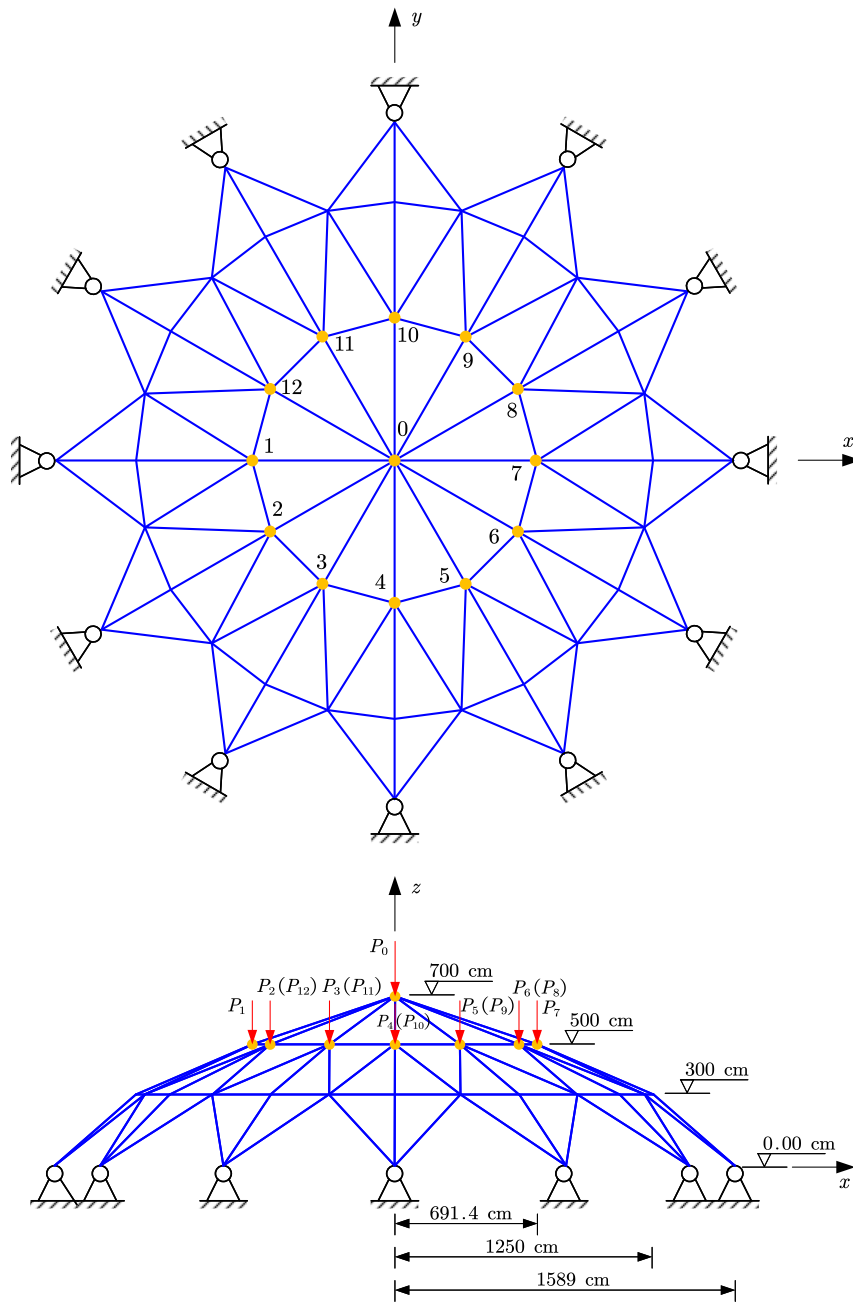


Fig. 15. A 120-bar space truss structure subject to thirteen vertical loads.

5.4. Example 4: A spatial steel frame structure with viscous dampers under fully nonstationary stochastic ground motion

To further demonstrate the practical applicability of the proposed methods, this example considers a two-bay, four-storey nonlinear spatial steel frame structure with three viscous dampers subjected to fully nonstationary ground motion, as shown in Fig. 18 [61]. The structure is modelled and analysed using the OpenSEES software (Version: 3.2.2-x64). In this model, the floor slabs are assumed to be rigid, with the IPE270 beams and IPB300 columns used. The column mass is taken as its self-weight, while the beam mass is defined as “self-weight of beam + dead loads  $D_L$  +  $0.2 \times$  live loads  $L_L$ ”. Steel material behaviour follows a bilinear stress–strain model (Fig. 18). The viscous dampers on the first floor are modelled using the Maxwell model, which consists of a linear spring and a nonlinear dashpot in series, with three coefficients: axial elastic stiffness of the linear spring ( $K_d$ ), damping

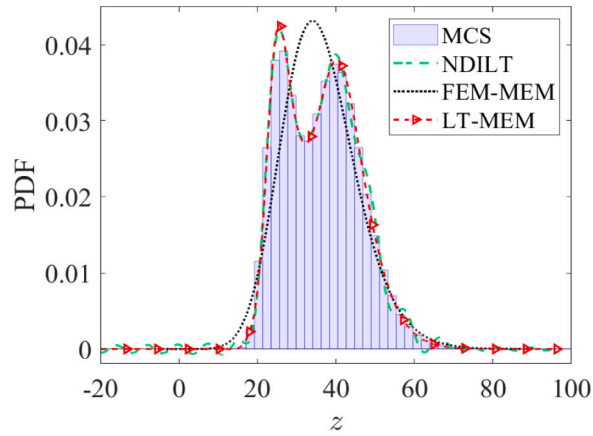


Fig. 16. PDF of Z in Example 3.

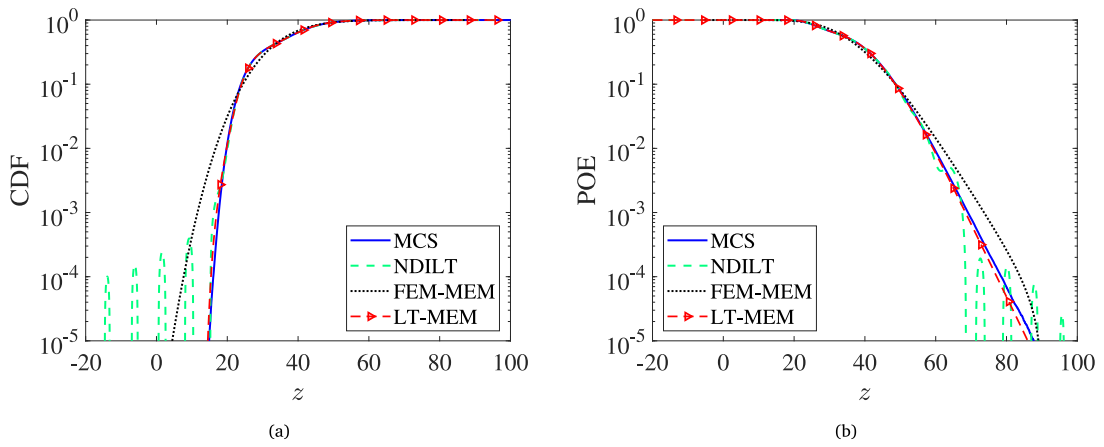


Fig. 17. (a) CDF and (b) POE of Z in Example 3.

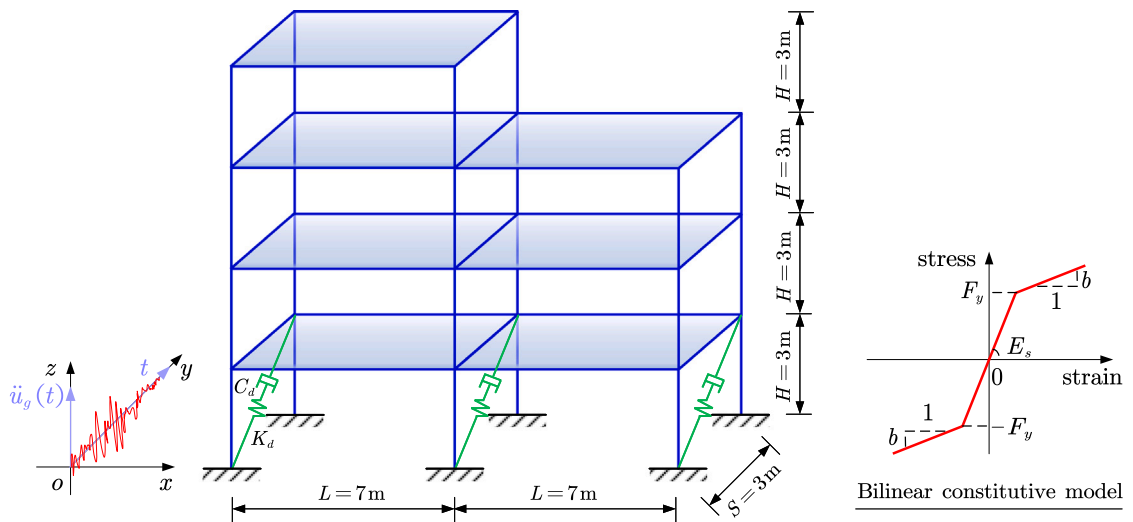
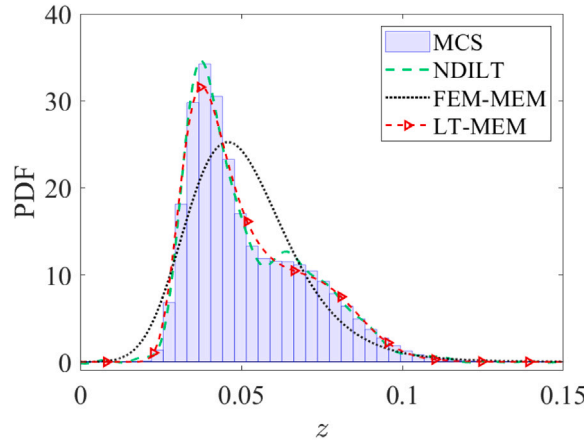


Fig. 18. A two-bay four-storey nonlinear spatial steel frame structure with viscous dampers.

**Table 5**  
Basic random variables for Example 4.

Variable	Description	Distribution	Mean	C.O.V	Weights
$D_L$	Dead load	Lognormal	10 N/m <sup>2</sup>	0.05	1
$L_L$	Live load	Lognormal	10 N/m <sup>2</sup>	0.1	1
$F_y$	Yield strength of the steel	Normal	250 MPa	0.15	1
$E_s$	Young's modulus of the steel	Gaussian mixture	[1, 2.3 ] ×10 <sup>5</sup> MPa	[0.1, 0.1]	[0.4, 0.6]
$b$	Strain-hardening ratio	Normal	0.001	0.05	1
$K_d$	Axial stiffness of linear spring	Normal	25 Pa	0.1	1
$C_d$	Damping coefficient	Normal	20.7452	0.1	1
$\alpha_d$	Velocity exponent	Normal	0.35	0.05	1
$\xi_1 \sim \xi_{1024}$	Random variables of random ground motions	Standard normal	0	–	1



**Fig. 19.** PDF of  $Z$  in Example 4.

coefficient ( $C_d$ ), and velocity exponent ( $\alpha_d$ ). Rayleigh damping is applied with damping ratios of 0.03 for both the first and second modes.

The non-stationary ground motions are considered as the external excitation of structures and modelled using Expansion Optimal Linear Estimation (EOLE) method [62,63]. Based on EOLE, the random ground motions  $\ddot{U}_g(t)$  can be expressed as follows

$$\ddot{U}_g(t) \approx \mu_{\ddot{U}_g(t)} + \sum_{i=1}^{N_t} \frac{\xi_i}{\sqrt{\theta_i}} \psi_i^T C_{\ddot{U}_g}, \tag{47}$$

where  $\mu_{\ddot{U}_g(t)}$  represents the mean of random ground motions (which is zero);  $N_t$  denotes the total number of discrete times and the truncation orders;  $\xi_i$ s are the independent standard normal random variables;  $\theta_i$  and  $\psi_i$  denote the eigenvalues and eigenvectors of  $C_{\ddot{U}_g}$ , respectively; and  $C_{\ddot{U}_g}$  is the covariance matrix with elements  $C_{\ddot{U}_g}(t_{\bar{k}}, t_{\bar{m}})$ , ( $\bar{k}, \bar{m} = 1, 2, \dots, N_t$ ). Further details on the EOLE method can be found in Appendix B and Ref. [63].

In this example, the ground motions  $\ddot{U}_g(t)$  are discretized into  $N_t = 1024$  time steps, meaning 1024 independent standard normal random variables are involved. As a result, a total of 1032 basic random variables are involved in this structure, capturing both the randomness of external loads and structural properties, and are listed in Table 5. Then, the representative point set  $\mathcal{P}_\theta$  in the 1032-dimensional random variable space is generated according to Eq. (A.4). Given the ultra-high dimensionality, 1500 points are used for this example.

First, the maximum absolute inter-storey drift of the whole structure, denoted by  $Z$ , is considered the quantity of interest. The parameters for LT-MEM are configured as follows:  $[\hat{a}_L, \hat{a}_U] = [-4.4, 4.4]$ ,  $[\hat{b}_L, \hat{b}_U] = [-10, -10]$ ,  $[\hat{\lambda}_L, \hat{\lambda}_U] = [-50, -50]$ ,  $L = 6$  and  $J = 4$ . Using the proposed methods with 1500 runs, the PDF, CDF and POE curves of  $Z$  are calculated and illustrated in Figs. 19 and 20. For comparison, the results from the FEM-MEM (1500 runs) are also included, along with benchmark results from MCS ( $1 \times 10^6$  runs). The proposed methods closely align with the MCS benchmarks, while the FEM-MEM results exhibit significant deviation.

The displacement of the top storey of the structure, denoted by  $Z$ , is analysed next. The PDF, CDF, and POE curves for the top storey's displacement at three specific time instants calculated by the proposed methods are shown in Figs. 21, 22 and 23, respectively. The parameter configurations for LT-MEM at these three time instants are summarized in Table 6. Additionally, the LT-MEM is utilized to capture the evolution of the PDF for the top storey's displacement. Fig. 24 illustrates this PDF evolution over the time interval [0, 15] seconds, along with the Kullback–Leibler divergence between the results obtained from LT-MEM and MCS at each time instant. The strong agreement between these results computed by the proposed methods and those from MCS

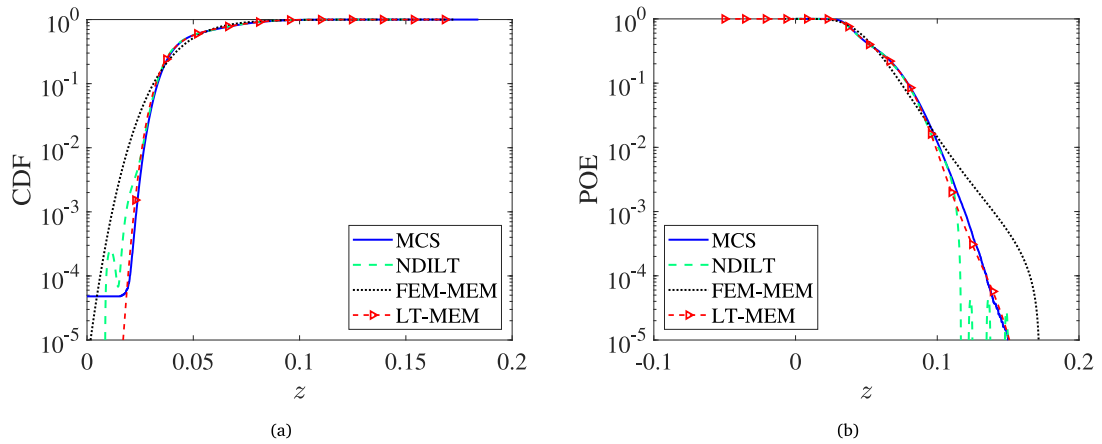


Fig. 20. (a) CDF and (b) POE of  $Z$  in Example 4.

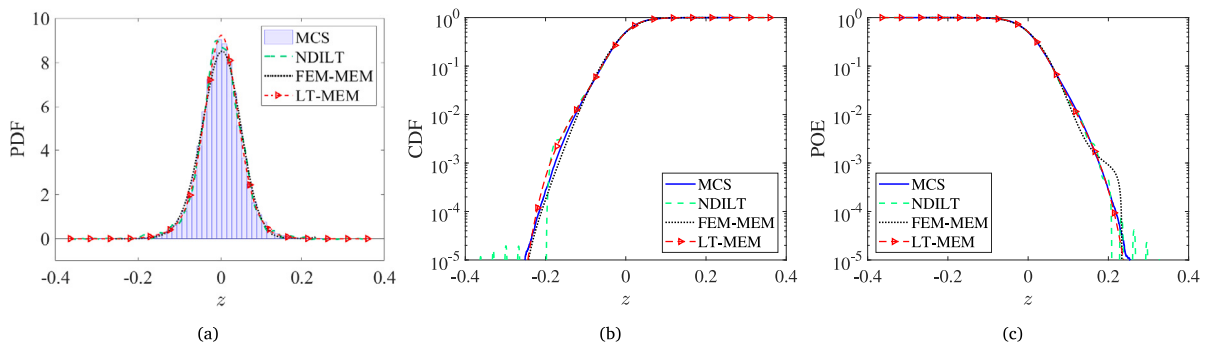


Fig. 21. (a) PDF, (b) CDF and (c) POE of top floor drift at 6 s in Example 4.

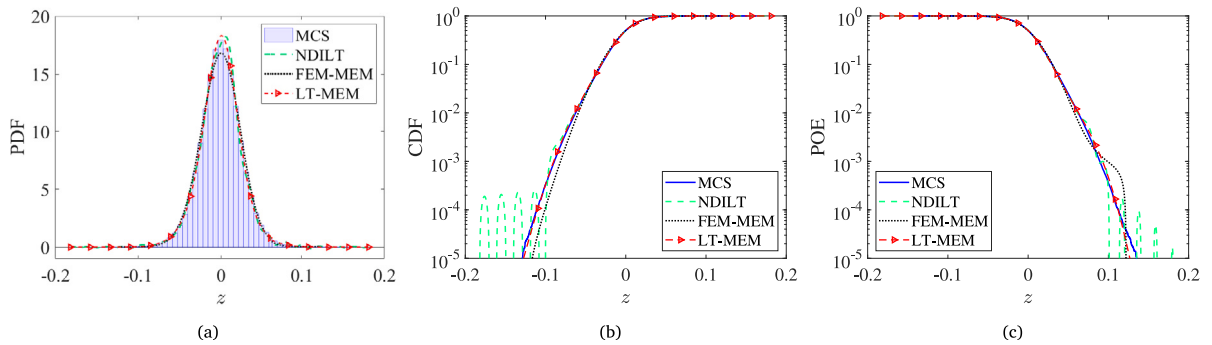


Fig. 22. (a) PDF, (b) CF and (c) POE of top floor drift at 12 s in Example 4.

demonstrates the effectiveness of the proposed methods for high-dimensional stochastic dynamic analysis of structures, underscoring their accuracy and efficiency.

### 6. Concluding remarks

This work explores the powerful capabilities of the LT and ILT for estimating complex-shaped output probability distributions in stochastic static and dynamic systems, accounting for uncertainties arising from both system parameters and external excitations. Specifically, we propose two efficient methods, NDILT and LT-MEM, for reconstructing output distributions, with a particular focus on handling intricate distributions. DILT, derived by decomposing the ILT that incorporates Euler's formula, provides a new analytic

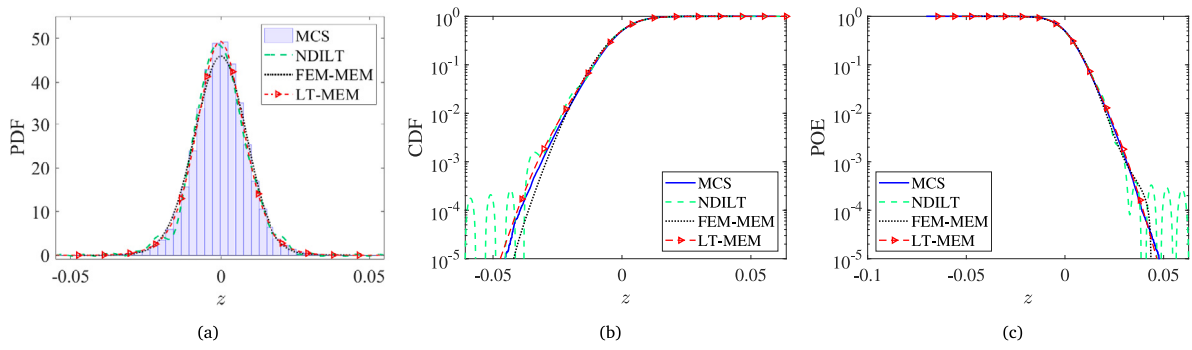


Fig. 23. (a) PDF, (b) CDF and (c) POE of top floor drift at 18 s in Example 4.

**Table 6**  
Parameters configuration of LT-MEM for Example 4.

Time instant	Optimization bounds			Parameter	
	$[\hat{\lambda}_L, \hat{\lambda}_U]$	$[\hat{a}_L, \hat{a}_U]$	$[\hat{b}_L, \hat{b}_U]$	$L$	$J$
6s		$[-5.4, 5.4]$			
12s	$[-50, 50]$	$[-5.3, 5.3]$	$[-10, 10]$	3	4
18s		$[-0.7, 0.7]$			

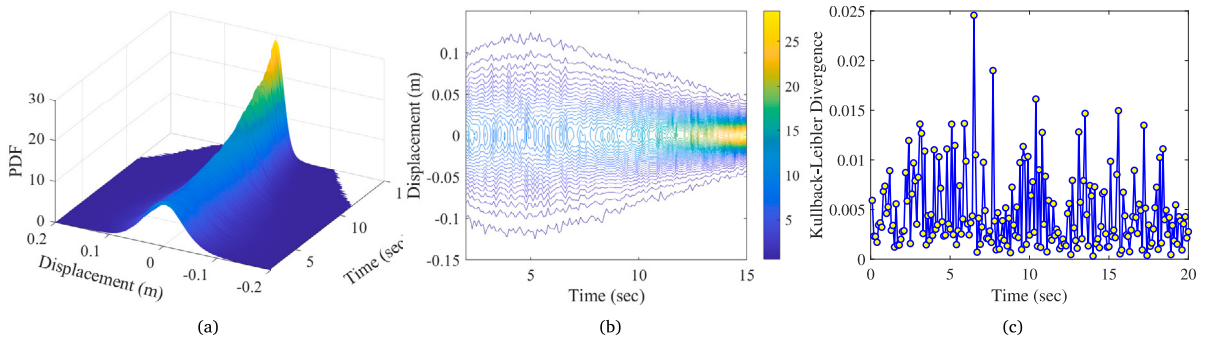


Fig. 24. (a) PDF, (b) Contour of PDF and (c) relative entropy of PDF of top floor drift of dynamical response in Example 4.

expression for unknown PDFs. Leveraging the rigorous theoretical foundation of DILT and the accurate estimation of RCLT and ICLT from reasonable sample sizes, the numerical algorithm of DILT, i.e., NDILT, offers a highly flexible approach for estimating the main body of PDFs with complex shapes using limited data. However, NDILT may exhibit oscillations and negative values in the tail region, making it particularly ideal for cases where the distribution tail is not a primary concern. On the other hand, inspired by the information-rich RCLT, LT-MEM leverages the RCLT as the constraint in the maximum entropy framework. This approach enables accurate reconstruction of probability distributions over their full domain, including both the main body and tails, and extends traditional MEM for complex-shaped distribution. LT-MEM addresses NDILT’s limitations, making it particularly effective for applications requiring precise tail estimation, such as reliability analysis. Some analytical distributions and numerical examples are studied to verify the effectiveness of the proposed methods. The results indicate that the proposed methods are applicable to both explicit and implicit problems. Furthermore, the proposed methods mitigate the “curse of dimensionality” to some extent, making them applicable to high-dimensional problems while balancing both accuracy and efficiency. For general problems with random inputs ranging from low- to high-dimensional, the proposed methods can estimate complex probability distributions with satisfactory accuracy, using approximately one thousand samples.

The proposed methods exhibit strong potential as a valuable tool for uncertainty characterization and propagation in complex problems, though some limitations need to be enhanced in future research. NDILT, despite its simplicity and flexibility, faces tail oscillation and non-positivity issues that require further careful investigation. LT-MEM avoids tail oscillations and non-positivity but at the cost of reduced flexibility for multi-modal PDFs. Determining the estimated bounds of the optimization parameter in LT-MEM remains empirical, particularly for parameter  $\alpha$ . Future work should focus on refining parameter determination strategies and enhancing the robustness of LT-MEM.

## CRedit authorship contribution statement

**Yang Zhang:** Writing – review & editing, Writing – original draft, Visualization, Validation, Methodology, Investigation, Conceptualization. **Chao Dang:** Writing – review & editing, Validation, Resources, Methodology, Investigation, Conceptualization. **Jun Xu:** Writing – review & editing, Supervision, Project administration, Funding acquisition. **Michael Beer:** Writing – review & editing, Validation, Supervision.

## Declaration of competing interest

The authors declare that they have no known competing financial interests or personal relationships that could have appeared to influence the work reported in this paper.

## Acknowledgements

The first and third authors are grateful for the financial support of the Science and Technology Innovation Program of Hunan Province, China (No. 2022RC1176), the National Natural Science Foundation of China (No. 52278178), the Open Fund of the State Key Laboratory of Disaster Reduction in Civil Engineering, China (No. SLDRCE21-04), and the Natural Science Foundation of Hunan Province, China (No. 2022JJ20012) for this research.

## Appendix A. NGV-NTM

The NGV-NTM point set is based on the New Generating Vector construction method (NGV) and the Number-Theoretical Method (NTM) [52]. In the NGV-NTM, the initial two-dimensional NTM point set, denoted as  $\mathcal{P}_u = \{u_q = (u_{q,1}, u_{q,2}), q = 1, 2, \dots, n\}$ , consisting of  $n$  points within the two-dimensional unit cube space  $C^2 = [0, 1]^2$ , is determined first. This is achieved as follows [64]:

$$\begin{cases} Q_{q,i} \equiv qh_i \pmod{n} \\ u_{q,i} = (2Q_{q,i} - 1) / 2n \end{cases} \quad q = 1, 2, \dots, n; i = 1, 2, \quad (\text{A.1})$$

where  $h_i$  is the components of the generating vector  $\mathbf{h} = (h_1, h_2) \equiv (1, \hat{a}) \pmod{n}$ ;  $\hat{a}$  is the primitive root of the prime number  $n$ ; the integers  $h_i$  and  $\hat{a}^{i-1}$  are congruent modulo  $n$ . In this paper, the number of points in the point set  $\mathcal{P}_u$  is specific as  $n = 1597$ , and the primitive root is chosen as  $\hat{a} = 679$  [52]. Then, the points of  $\mathcal{P}_u$  can be generated using Eq. (A.1).

Second, the cutting strategy [12] is employed to obtain the two-dimensional cutting point set  $\mathcal{P}_{\hat{u}} = \{\hat{u}_{\hat{q}} = (\hat{u}_{\hat{q},1}, \hat{u}_{\hat{q},2}), \hat{q} = 1, 2, \dots, n_t\}$  with a user-defined number  $n_t$  of points (where  $0 < n_t \leq n$ ), achieving by cutting the point set  $\mathcal{P}_u$  using a square cutting region  $C_{\text{cut}}^2 = [0, u_{\text{cut}}]^2$ ,  $u_{\text{cut}} \in [0, 1]$ . Points  $u_q$  that fall within the square cutting region  $C_{\text{cut}}^2$  are selected as  $u_{\hat{q}}$ . The purpose of the cutting strategy is to generate a sparsified uniform point set. The algorithm details are provided in Algorithm 1.

---

### Algorithm 1 : Cutting method [12]

---

```

1: while  $\hat{n} < n_t$  do
2:   Increase the value of  $u_{\text{cut}}$ ;
   Calculate:  $\mathcal{P}_{\hat{u}} = \{\hat{u}_{\hat{q}} = (\hat{u}_{\hat{q},1}, \hat{u}_{\hat{q},2}), \hat{q} = 1, 2, \dots, \hat{n}\}$ 
3:    $= \{u_q \in \mathcal{P}_u : u_{q,1} < u_{\text{cut}} \cap u_{q,2} < u_{\text{cut}}, q = 1, 2, \dots, n\}$ ;
4: end while

```

---

Next, the NGV construction method [52] is implemented based on a TRSS to efficiently construct the generating vector, denoted as  $\mathbf{v} = (v_1, v_2, \dots, v_{\hat{q}}, \dots, v_{n_t}), \hat{q} = 1, 2, \dots, n_t; 0 < v_{\hat{q}} \leq n_t$ , for high-dimensional point sets, which is express as follows

$$\begin{cases} \hat{\mathbf{u}} = \text{sort}(\hat{\mathbf{u}}^{(2)}) \\ \mathcal{P}_{\hat{\mathbf{u}}} = f_{\hat{\mathbf{u}}^{(2)}}^{-1}(\hat{\mathbf{u}}) \end{cases}, \quad (\text{A.2})$$

$$\begin{cases} \hat{\mathcal{P}} = \text{sort}(\mathcal{P}_{\hat{\mathbf{u}}}) \\ \mathbf{v} = f_{\hat{\mathcal{P}}}^{-1}(\hat{\mathcal{P}}) \end{cases}, \quad (\text{A.3})$$

where Eqs. (A.2) and (A.3) refer to the first and second rounds of sorting operations, respectively. In Eq. (A.2),  $\hat{\mathbf{u}}^{(2)}$  represents the second dimension of the cutting point set  $\mathcal{P}_{\hat{\mathbf{u}}}$ . The function  $\text{sort}(\cdot)$  arranges elements in ascending order, and  $\hat{\mathbf{u}} = (\hat{u}_1, \hat{u}_2, \dots, \hat{u}_{\hat{q}}, \dots, \hat{u}_{n_t})$  is the sorted version of  $\hat{\mathbf{u}}^{(2)}$ . The set  $\mathcal{P} = [1, 2, \dots, n_t]$  indicates the positions of each element  $\hat{u}_{\hat{q},2}$  in  $\hat{\mathbf{u}}^{(2)}$ . The function  $f_{\hat{\mathbf{u}}^{(2)}}$  maps  $\mathcal{P}$  to  $\hat{\mathbf{u}}^{(2)}$  and its inverse is denoted as  $f_{\hat{\mathbf{u}}^{(2)}}^{-1}(\cdot)$ . In Eq. (A.3),  $\mathcal{P}_{\hat{\mathbf{u}}}$  represents the positions of the sorted elements  $\hat{u}_{\hat{q}}$  in  $\hat{\mathbf{u}}^{(2)}$ , while  $f_{\hat{\mathcal{P}}}$  defines a function mapping  $\mathcal{L}$  to  $\mathcal{P}_{\hat{\mathbf{u}}}$ , where  $\mathcal{L}$  contains the positions of each element in  $\mathcal{P}_{\hat{\mathbf{u}}}$ . The inverse function is expressed as  $f_{\hat{\mathcal{P}}}^{-1}(\cdot)$ .

**Table B.7**  
Parameters in the PSD and the time–frequency–modulation function (Example 4).

Item	$\bar{a}_{\max}^2$ (cm/s <sup>2</sup> )	$\zeta_g$ (rad/s)	$t_g$	$\zeta_f$ (rad/s)	$t_f$	$\bar{r}$	$\eta$	$\varpi$	$\hat{\kappa}$
Value	150	$8\pi$	0.60	$0.8\pi$	0.6	2.95	0.240	0.241	0.005

Note:  $\varpi = \eta + 0.001$

Finally, the NGV-NTM point set  $\mathcal{P}_{\tilde{u}} = \{\tilde{u}_{\tilde{q}} = (\tilde{u}_{\tilde{q},1}, \tilde{u}_{\tilde{q},2}, \dots, \tilde{u}_{\tilde{q},d}), \tilde{q} = 1, 2, \dots, n_t\}$  in the  $d$ -dimensional unit hypercube space  $C^d = [0, 1]^d$  can be recursively derived by the dimension-by-dimension mapping as follows [52,65]

$$\begin{cases} \tilde{u}_{\tilde{q},i} = \frac{2\tilde{q} - 1}{2n_t}, & i = 1 \\ \tilde{u}_{\tilde{q},i} = \tilde{u}_{v_{\tilde{q},i-1}}, & i = 2, 3, \dots, d \end{cases}, \tilde{q} = 1, 2, \dots, n_t, \tag{A.4}$$

where  $\tilde{u}_{\tilde{q},i}$  is the  $\tilde{q}$ th point of the  $i$ th dimension in the NGV-NTM point set  $\mathcal{P}_{\tilde{u}}$  and  $\tilde{u}_{v_{\tilde{q},i-1}}$  is the  $v_{\tilde{q}}$ th point of the  $(i - 1)$ th dimension of  $\mathcal{P}_{\tilde{u}}$ .

Once the NGV-NTM point set  $\mathcal{P}_{\tilde{u}}$  is obtained, it can be transformed into the representative point set  $\mathcal{P}_{\theta} = \{\theta_{\tilde{q}} = (\theta_{\tilde{q},1}, \theta_{\tilde{q},2}, \dots, \theta_{\tilde{q},d}), \tilde{q} = 1, 2, \dots, n_t\}$  in the  $d$ -dimensional original random-variate space  $\Omega_{\Theta}$  through the isoprobabilistic transformation

$$\theta_{\tilde{q}}^{(i)} = F^{-1}(\mathcal{Y}_{\tilde{u}}(\tilde{u}_{\tilde{q},i})) = F^{-1}(\tilde{u}_{\tilde{q},i}), i = 1, 2, \dots, d; \tilde{q} = 1, 2, \dots, n_t, \tag{A.5}$$

where  $F^{-1}(\cdot)$  represents the inverse CDF of random variable in  $\Theta = [\theta_1, \theta_2, \dots, \theta_d]$ ; and  $\mathcal{Y}_{\tilde{u}}(\cdot)$  denotes the CDF of the uniform distribution with parameter  $[0, 1]$ .

**Appendix B. Details of EOLE in the Example 4**

In EOLE (Eq. (47)), the covariance matrix  $C_{\tilde{U}_g}$  can be calculated as the inverse Fourier transform of its Power Spectrum Density (PSD), which is given by

$$C_{\tilde{U}_g}(t_{\bar{k}}, t_{\bar{m}}) \approx \int_{-\zeta_u}^{+\zeta_u} \mathcal{A}(t_{\bar{k}}, \zeta) \mathcal{A}(t_{\bar{m}}, \zeta) S(\zeta) \exp(i\zeta\tau) d\zeta, (\bar{k}, \bar{m} = 1, 2, \dots, N_t), \tag{B.1}$$

where  $\zeta$  represents the frequency; the upper cut-off frequencies  $\zeta_u$  is set to  $\zeta_u = 50\pi$  [63];  $\tau$  denotes the time difference;  $S(\zeta)$  is the classic Clough–Penzien PSD;  $\mathcal{A}(t, \zeta)$  is the time–frequency modulation function accounting for non-stationarity. The expressions for  $S(\zeta)$  and  $\mathcal{A}(t, \zeta)$  are as follows

$$S(\zeta) = \frac{\zeta_g^4 + 4t_g^2 \zeta_g^2 \zeta^2}{(\zeta_g^2 - \zeta^2)^2 + 4t_g^2 \zeta_g^2 \zeta^2} \frac{\zeta^4}{(\zeta_f^2 - \zeta^2)^2 + 4t_f^2 \zeta_f^2 \zeta^2} \frac{\bar{a}_{\max}^2}{\pi \zeta_g \left(2t_g + \frac{1}{2t_g}\right)}, \tag{B.2}$$

$$\mathcal{A}(t, \zeta) = \frac{\exp(-\eta t) - \exp\left(-\left(\hat{\kappa} \left|\zeta - \zeta_g\right| + \varpi\right)t\right)}{\exp(-\eta t^*) - \exp\left(-\left(\hat{\kappa} \left|\zeta - \zeta_g\right| + \varpi\right)t^*\right)}, t > 0, \zeta > 0 \tag{B.3}$$

$$t^* = \frac{\ln\left(\hat{\kappa} \left|\zeta - \zeta_g\right| + \varpi\right) - \ln \eta}{\hat{\kappa} \left|\zeta - \zeta_g\right| + (\varpi - \eta)}.$$

The specific values for these parameters in Eqs. (B.1)–(B.3) are listed in Table B.7 [63,66].

**Data availability**

No data was used for the research described in the article.

**References**

- [1] X. Wang, Y. Zhao, Q. Ni, S. Tang, Nonparametric density estimation with nonuniform B-spline bases, *J. Comput. Appl. Math.* 440 (2024) 115648.
- [2] J. Xu, Q. Yu, Harmonic transform-based non-parametric density estimation method for forward uncertainty propagation and reliability analysis, *Struct. Saf.* 103 (2023) 102331.
- [3] E. Parzen, On estimation of a probability density function and mode, *Ann. Math. Stat.* 33 (1962) 1065–1076.
- [4] J.-Q. Chen, Y.-L. He, Y.-C. Cheng, P. Fournier-Viger, J.Z. Huang, A multiple kernel-based kernel density estimator for multimodal probability density functions, *Eng. Appl. Artif. Intell.* 132 (2024) 107979.
- [5] A. Majdara, S. Nooshabadi, Nonparametric density estimation using copula transform, Bayesian sequential partitioning, and diffusion-based kernel estimator, *IEEE Trans. Knowl. Data Eng.* 32 (4) (2019) 821–826.
- [6] Y. Zhao, M. Zhang, Q. Ni, X. Wang, Adaptive nonparametric density estimation with B-spline bases, *Mathematics* 11 (2) (2023) 291.
- [7] J.L. Kirkby, Á. Leitao, D. Nguyen, Nonparametric density estimation and bandwidth selection with B-spline bases: A novel Galerkin method, *Comput. Statist. Data Anal.* 159 (2021) 107202.

- [8] J. Li, J.B. Chen, Probability density evolution method for dynamic response analysis of structures with uncertain parameters, *Comput. Mech.* 34 (5) (2004) 400–409.
- [9] J. Li, J.-B. Chen, The dimension-reduction strategy via mapping for probability density evolution analysis of nonlinear stochastic systems, *Probabilistic Eng. Mech.* 21 (4) (2006) 442–453.
- [10] J. Li, J. Chen, The principle of preservation of probability and the generalized density evolution equation, *Struct. Saf.* 30 (1) (2008) 65–77.
- [11] M.-Z. Lyu, D.-C. Feng, J.-B. Chen, J. Li, A decoupled approach for determination of the joint probability density function of a high-dimensional nonlinear stochastic dynamical system via the probability density evolution method, *Comput. Methods Appl. Mech. Engrg.* 418 (2024) 116443.
- [12] Y. Zhang, J. Xu, A partial decomposition cutting method with CF-discrepancy for points selection in stochastic seismic analysis of structures, *Struct. Saf.* 111 (2024) 102513.
- [13] C. Lemieux, *Monte Carlo and Quasi-Monte Carlo Sampling*, vol. 20, Springer, 2009.
- [14] M.D. Shields, K. Teferra, A. Hapij, R.P. Daddazio, Refined stratified sampling for efficient Monte Carlo based uncertainty quantification, *Reliab. Eng. Syst. Saf.* 142 (2015) 310–325.
- [15] P. Bratley, B.L. Fox, Algorithm 659: Implementing sobol's quasirandom sequence generator, *ACM Trans. Math. Software* 14 (1) (1988) 88–100.
- [16] J. Xu, J. Song, Q. Yu, F. Kong, Generalized distribution reconstruction based on the inversion of characteristic function curve for structural reliability analysis, *Reliab. Eng. Syst. Saf.* 229 (2023) 108768.
- [17] Y.-Y. Weng, T. Liu, X.-Y. Zhang, Y.-G. Zhao, Probability density estimation of polynomial chaos and its application in structural reliability analysis, *Reliab. Eng. Syst. Saf.* 253 (2025) 110537.
- [18] Y. Peng, T. Zhou, J. Li, Surrogate modeling immersed probability density evolution method for structural reliability analysis in high dimensions, *Mech. Syst. Signal Process.* 152 (2021) 107366.
- [19] G. Chen, D. Yang, Direct probability integral method for stochastic response analysis of static and dynamic structural systems, *Comput. Methods Appl. Mech. Engrg.* 357 (2019) 112612.
- [20] G. Chen, D. Yang, Y. Liu, H. Guo, System reliability analyses of static and dynamic structures via direct probability integral method, *Comput. Methods Appl. Mech. Engrg.* 388 (2022) 114262.
- [21] L. Li, G. Chen, M. Fang, D. Yang, Reliability analysis of structures with multimodal distributions based on direct probability integral method, *Reliab. Eng. Syst. Saf.* 215 (2021) 107885.
- [22] Q. Yu, J. Xu, Harmonic transform-based density estimation method for uncertainty propagation and reliability analysis involving multi-modal distributions, *Mech. Syst. Signal Process.* 190 (2023) 110113.
- [23] Q. Yu, J. Xu, Distribution reconstruction and reliability assessment of complex LSFs via an adaptive non-parametric density estimation method, *Reliab. Eng. Syst. Saf.* (2024) 110609.
- [24] C. Dang, M.A. Valdebenito, N.A. Manque, J. Xu, M.G. Faes, Response probability distribution estimation of expensive computer simulators: A Bayesian active learning perspective using Gaussian process regression, *Struct. Saf.* 114 (2025) 102579.
- [25] J. Xu, Y. Zhang, C. Dang, A novel hybrid cubature formula with pearson system for efficient moment-based uncertainty propagation analysis, *Mech. Syst. Signal Process.* 140 (2020) 106661.
- [26] J. Xu, C. Dang, A new bivariate dimension reduction method for efficient structural reliability analysis, *Mech. Syst. Signal Process.* 115 (2019) 281–300.
- [27] M. Choi, B. Sweetman, The Hermite moment model for highly skewed response with application to tension leg platforms, *J. Offshore Mech. Arct. Eng.* 132 (2) (2010) 021602.
- [28] B. Huang, X. Du, Uncertainty analysis by dimension reduction integration and saddlepoint approximations, *J. Mech. Des.* 128 (1) (2005) 26–33.
- [29] J. Xu, C. Dang, F. Kong, Efficient reliability analysis of structures with the rotational quasi-symmetric point- and the maximum entropy methods, *Mech. Syst. Signal Process.* 95 (2017) 58–76.
- [30] W. He, Y. Zeng, G. Li, A novel structural reliability analysis method via improved maximum entropy method based on nonlinear mapping and sparse grid numerical integration, *Mech. Syst. Signal Process.* 133 (2019) 106247.
- [31] J. Xu, F. Kong, Adaptive scaled unscented transformation for highly efficient structural reliability analysis by maximum entropy method, *Struct. Saf.* 76 (2019) 123–134.
- [32] J. Xu, S. Zhu, An efficient approach for high-dimensional structural reliability analysis, *Mech. Syst. Signal Process.* 122 (2019) 152–170.
- [33] G. Li, C. Zhou, Y. Zeng, W. He, H. Li, R. Wang, New maximum entropy-based algorithm for structural design optimization, *Appl. Math. Model.* 66 (2019) 26–40.
- [34] X. Zhang, M.D. Pandey, Structural reliability analysis based on the concepts of entropy, fractional moment and dimensional reduction method, *Struct. Saf.* 43 (2013) 28–40.
- [35] G. Li, W. He, Y. Zeng, An improved maximum entropy method via fractional moments with Laplace transform for reliability analysis, *Struct. Multidiscip. Optim.* 59 (2019) 1301–1320.
- [36] J. Xu, C. Dang, A novel fractional moments-based maximum entropy method for high-dimensional reliability analysis, *Appl. Math. Model.* 75 (2019) 749–768.
- [37] Y. Zhang, J. Xu, M. Beer, A single-loop time-variant reliability evaluation via a decoupling strategy and probability distribution reconstruction, *Reliab. Eng. Syst. Saf.* 232 (2023) 109031.
- [38] Y. Zhang, J. Xu, P. Gardoni, A loading contribution degree analysis-based strategy for time-variant reliability analysis of structures under multiple loading stochastic processes, *Reliab. Eng. Syst. Saf.* 243 (2024) 109833.
- [39] Z. Zhang, C. Jiang, X. Han, X.X. Ruan, A high-precision probabilistic uncertainty propagation method for problems involving multimodal distributions, *Mech. Syst. Signal Process.* 126 (2019) 21–41.
- [40] G. Li, Y.X. Wang, Y. Zeng, W.X. He, A new maximum entropy method for estimation of multimodal probability density function, *Appl. Math. Model.* 102 (2022) 137–152.
- [41] G. Li, Y. Wang, W. He, C. Zhong, Y. Wang, A data-driven maximum entropy method for probability uncertainty analysis based on the B-spline theory, *Probabilistic Eng. Mech.* 78 (2024) 103688.
- [42] W. He, Y. Wang, G. Li, J. Zhou, A novel maximum entropy method based on the B-spline theory and the low-discrepancy sequence for complex probability distribution reconstruction, *Reliab. Eng. Syst. Saf.* 243 (2024) 109909.
- [43] S. He, J. Xu, Y. Zhang, Reliability computation via a transformed mixed-degree cubature rule and maximum entropy, *Appl. Math. Model.* 104 (2022) 122–139.
- [44] K. Reddy, K. Kumar, J. Satish, S. Vaithyasubramanian, A review on applications of Laplace transformations in various fields, *J. Adv. Res. Dyn. Control Syst.* 9 (14) (2017) 14–24.
- [45] K.L. Kuhlman, Review of inverse Laplace transform algorithms for Laplace-space numerical approaches, *Numer. Algorithms* 63 (2013) 339–355.
- [46] G. Horváth, I. Horváth, S.A.-D. Almousa, M. Telek, Numerical inverse Laplace transformation using concentrated matrix exponential distributions, *Perform. Eval.* 137 (2020) 102067.
- [47] A. Tagliani, Y. Velásquez, Inverse Laplace transform for heavy-tailed distributions, *Appl. Math. Comput.* 150 (2) (2004) 337–345.
- [48] L. Niu, M. Di Paola, A. Pirrotta, W. Xu, Laplace and mellin transform for reconstructing the probability distribution by a limited amount of information, *Probabilistic Eng. Mech.* 78 (2024) 103700.

- [49] H. Dai, Z. Ma, L. Li, An improved complex fractional moment-based approach for the probabilistic characterization of random variables, *Probabilistic Eng. Mech.* 53 (2018) 52–58.
- [50] M. Di Paola, F.P. Pinnola, Riesz fractional integrals and complex fractional moments for the probabilistic characterization of random variables, *Probabilistic Eng. Mech.* 29 (2012) 149–156.
- [51] A. Tagliani, Inverse two-sided Laplace transform for probability density functions, *J. Comput. Appl. Math.* 90 (2) (1998) 157–170.
- [52] Y. Zhang, J. Xu, E. Zio, A novel deterministic sampling approach for the reliability analysis of high-dimensional structures, *Struct. Saf.* 112 (2025) 102545.
- [53] E.T. Jaynes, Information theory and statistical mechanics, *Phys. Rev.* 106 (4) (1957) 620–630.
- [54] P. Neelakanta, J. Kapur, H. Kesavan, Entropy optimization principles with applications, 1992.
- [55] J. Xu, A new method for reliability assessment of structural dynamic systems with random parameters, *Struct. Saf.* 60 (2016) 130–143.
- [56] A. Rajan, Y.C. Kuang, M.P.-L. Ooi, S.N. Demidenko, H. Carstens, Moment-constrained maximum entropy method for expanded uncertainty evaluation, *IEEE Access* 6 (2018) 4072–4082.
- [57] D.P. Bertsekas, *Nonlinear Programming*, Athena Scientific, Belmont, MA, USA, 1995.
- [58] C. Dang, P. Wei, J. Song, M. Beer, Estimation of failure probability function under imprecise probabilities by active learning-augmented probabilistic integration, *ASCE-ASME J. Risk Uncertain. Eng. Syst. Part A: Civ. Eng.* 7 (4) (2021) 04021054.
- [59] C. Dang, P. Wei, M.G.R. Faes, M.A. Valdebenito, M. Beer, Parallel adaptive Bayesian quadrature for rare event estimation, *Reliab. Eng. Syst. Saf.* 225 (2022) 108621.
- [60] C. Dang, M.A. Valdebenito, P. Wei, J. Song, M. Beer, Bayesian active learning line sampling with log-normal process for rare-event probability estimation, *Reliab. Eng. Syst. Saf.* 246 (2024) 110053.
- [61] C. Ding, C. Dang, M.A. Valdebenito, M.G.R. Faes, M. Broggi, M. Beer, First-passage probability estimation of high-dimensional nonlinear stochastic dynamic systems by a fractional moments-based mixture distribution approach, *Mech. Syst. Signal Process.* 185 (2023) 109775.
- [62] C.-C. Li, A.D. Kiureghian, Optimal discretization of random fields, *J. Eng. Mech.* 119 (6) (1993) 1136–1154.
- [63] B. Peng, J. Xu, Y. Peng, Efficient simulation of multivariate non-stationary ground motions based on a virtual continuous process and EOLE, *Mech. Syst. Signal Process.* 184 (2023) 109722.
- [64] K. Fang, Y. Wang, *Number-Theoretic Methods in Statistics*, vol. 51, CRC Press, 1993.
- [65] K. Gao, G. Liu, W. Tang, High-dimensional reliability analysis based on the improved number-theoretical method, *Appl. Math. Model.* 107 (2022) 151–164.
- [66] Z. Liu, Z. Liu, X. Ruan, Q. Zhang, Spectral representation-based dimension reduction for simulating multivariate non-stationary ground motions, *Soil Dyn. Earthq. Eng.* 114 (2018) 313–325.